

Compact S/X Dual-Band Coaxial-Fed CP Polarizer for Satellite Communications

by

Bradden K. Cowan

A Thesis Presented in Partial Fulfillment  
of the Requirements for the Degree  
Master of Science

Approved November 2021 by the  
Graduate Supervisory Committee:

James Aberle, Chair  
Georgios Trichopoulos  
George Pan

ARIZONA STATE UNIVERSITY

December 2021

## ABSTRACT

Satellite communications employs circular polarization (CP) to circumvent the well-known phenomenon known as Faraday Rotation, where the ionosphere rotates the horizontal and vertical polarization components resulting in signal degradation especially at lower frequencies, i.e., VHF and L-band, and in tropical regions of the earth.

Satellite circularly polarized antenna feed technology commonly employs bulky and lossy 90-degree hybrid combiners to convert linear polarization to circular polarization, which results in a higher noise figure for receive applications and a less repeatable and more difficult design to tune and manufacture.

This thesis aims at designing, modeling and simulating a prototype S/X dual band CP feed/polarizer utilizing a technique known as the “Spread-Squeeze” polarizer, which offers the advantages of compact size, ease of manufacture, and lower loss and noise figure, relative to the current technology that often employs an external 3-dB hybrid combiner. Ansys High Frequency Structure Simulator (HFSS), a commercial electromagnetic modeling and simulation tool, is used for the simulations.

Further, this thesis aims to characterize the performance of the dual feed horn with respect to aperture efficiency, that is, the degree to which the feed horn illuminates the parabolic reflector.

## DEDICATION

*This is dedicated, first and foremost, to my Lord and Saviour Jesus Christ, who though he was rich, yet for our sakes became poor, that we through his poverty might be rich; to my dear wife, without whose support, encouragement and patience, this would not have been possible; and to my parents, my mother for encouraging me to pursue my college education, and my father for inspiring me to be everything I can be.*

## ACKNOWLEDGMENTS

I would like to sincerely thank Professor James Aberle for the opportunity to do a thesis project of this nature, for his patience and encouragement, and for his expert guidance and understanding of the subject matter.

# TABLE OF CONTENTS

	Page
LIST OF TABLES .....	vi
LIST OF FIGURES .....	vii
LIST OF EQUATIONS .....	xi
CHAPTER	
1 INTRODUCTION .....	1
1.1 Linear Polarization .....	1
1.2 Circular Polarization .....	2
1.3 Circular Polarized Feed Horns .....	3
1.4 Advantages of Circular Polarization in Satellite Communications.....	4
1.4.1 The Faraday Effect.....	4
1.4.2 Atmospheric Conditions .....	5
1.4.3 Easier installation.....	5
1.4.4 Higher link reliability.....	6
2 THEORETICAL BACKGROUND.....	7
2.1 Linear to Circular Polarizer .....	7
2.2 Commercial versions for comparison .....	8
2.3 Spread-Squeeze Waveguide Polarizer .....	10

CHAPTER	Page
3 DESIGN AND OPTIMIZATION.....	12
3.1 Design Approach.....	12
3.2 Port to Port Isolation .....	15
3.3 Isolated X-, S-band Radiation Patterns and Input Impedance.....	16
4 FINAL RESULTS .....	21
4.1 Integrated X-band Performance .....	21
4.2 Integrated S-band Performance .....	36
4.3 Aligning Phase Centers for Integrated Dual S/X Band Horns .....	49
4.4 Aperture Efficiency .....	52
4.5 Dual Coax to Circular Waveguide Transition.....	62
5 CONCLUSION AND FUTURE WORK .....	63
REFERENCES .....	64
APPENDIX	
A MATLAB SCRIPT - APERTURE EFFICIENCY .....	66

## LIST OF TABLES

Table	Page
1.1-1 Polarization Available on Intelsat Satellites .....	1
4.3-1 Phase Center Alignment .....	50

## LIST OF FIGURES

Figure	Page
1.1-1 Linear Polarization .....	1
1.2-1 Circular Polarization.....	2
1.4.1-1 Faraday’s Effect: The Linear Polarized Signal Twists.....	4
2.2-1 Commercial S/X Dual-band Feed Using External Hybrid Combiner .....	8
2.3-1 Spread-Squeeze Polarizer Conceptual Diagram.....	10
2.3-2 Conversion from Linear $TE_{11}$ to Circular $TE_{11}(v) \pm j TE_{11}(h)$ .....	11
3.1-1 Dual-band Coaxial Waveguide Dimensions.....	13
3.3-1 Isolated X-band Design .....	16
3.3-2. Calculated 3-D X-band RHCP Radiation Pattern (8450 MHz).....	17
3.3-3 Axial Ratio for Isolated X-band Horn ( $\Phi = \Theta = 0^\circ$ ).....	17
3.3-4 $S_{11}$ (Mode1/Mode2) Calculated Impedance Match of the X-Band Port. ....	18
3.3-5 Feed Boresight Axis View. Four Probes Are Fed with Phase Shifted Signals .....	18
3.3-6 S-band Horn Modeled in HFSS.....	19
3.3-7 Calculated S-band 3-D Radiation Pattern.....	20
3.3-8 Calculated S-band Axial Ratio for $\Phi = 0$ Deg. ....	20
4.1-1 Integrated X-band and S-band Horns (HFSS).....	21
4.1-2 Integrated S/X Band Horn (HFSS).....	22
4.1-3 X-band Mode 1 Port Fields .....	23
4.1-4 Integrated X-band Longitudinal Mag E Fields.....	24
4.1-5 Integrated X-band Mode 1 Axial Ratio .....	25
4.1-6 Integrated X-band Mode 2 Axial Ratio .....	25



Figure	Page
4.1-7 X-band 3-D Polar Plot (RHCP, Low-band, 8400 MHz) .....	26
4.1-8 X-band 3-D Polar Plot (RHCP, Mid-band, 8450 MHz) .....	26
4.1-9 X-band 3-D Polar Plot (RHCP, High-band, 8500 MHz).....	27
4.1-10 X-band 3-D Polar Plot (LHCP, Low-band, 8400 MHz).....	28
4.1-11 X-band 3-D Polar Plot (LHCP, Mid-band, 8450 MHz) .....	28
4.1-12 X-band 3-D Polar Plot (LHCP, High-band, 8500 MHz).....	29
4.1-13. X-band RHCP 2-D Radiation Pattern ( $\Phi = 0^\circ, 90^\circ, 8400 \text{ MHz}$ ) .....	30
4.1-14 X-band RHCP 2-D Radiation Pattern ( $\Phi = 0^\circ, 90^\circ, 8450 \text{ MHz}$ ) .....	30
4.1-15 X-band RHCP 2-D Radiation Pattern ( $\Phi = 0^\circ, 90^\circ, 8500 \text{ MHz}$ ) .....	31
4.1-16 X-band LHCP 2-D Radiation Pattern ( $\Phi = 0^\circ, 90^\circ, 8400 \text{ MHz}$ ) .....	32
4.1-17 X-band LHCP 2-D Radiation Pattern ( $\Phi = 0^\circ, 90^\circ, 8450 \text{ MHz}$ ) .....	32
4.1-18 X-band LHCP 2-D Radiation Pattern ( $\Phi = 0^\circ, 90^\circ, 8500 \text{ MHz}$ ) .....	33
4.1-19 Integrated X-band Input Return Loss Mode1 Incident.....	34
4.1-20 Integrated X-band Input Return Loss Mode2 Incident.....	34
4.1-21 Isolation at S-band Due to X-band Mode1, Mode2 Incident .....	35
4.2-1 Integrated S-band Port Fields .....	36
4.2-2 Integrated S-band Longitudinal Mag E Fields .....	37
4.2-3 Integrated S-band Axial Ratio (Mode1, $TE_{11}$ ).....	38
4.2-4 Integrated S-band Mode2, $TE_{11}$ Axial Ratio .....	38
4.2-5 Integrated S-band Input Return Loss (Mode1 Incident).....	39
4.2-6 Isolation at X-band Port1, Port2 Due to S-band Port2 (Mode1) Incident .....	39
4.2-7 Integrated S-band Input Return Loss (Mode2 Incident).....	40

Figure	Page
4.2-8 Isolation at X-band Port1, Port2 Due to S-band Port3 (Mode2) Incident .....	40
4.2-9 Integrated S-band RHCP 3-D Polar Radiation Pattern (2200 MHz).....	41
4.2-10 Integrated S-band RHCP 3-D Polar Radiation Pattern (2350 MHz).....	41
4.2-11 Integrated S-band RHCP 3-D Polar Radiation Pattern (2500 MHz).....	42
4.2-12 Integrated S-band LHCP 3-D Polar Radiation Pattern (2200 MHz).....	43
4.2-13 Integrated S-band LHCP 3-D Polar Radiation Pattern (2350 MHz).....	43
4.2-14 Integrated S-band LHCP 3-D Polar Radiation Pattern (2500 MHz).....	44
4.2-15 Integrated S-band RHCP 2-D Pattern (Phi = 0°, 90°) at 2200 MHz .....	45
4.2-16 Integrated S-band RHCP 2-D Pattern (Phi = 0°, 90°) at 2350 MHz .....	45
4.2-17 Integrated S-band RHCP 2D Pattern (Phi = 0°, 90°) at 2500 MHz .....	46
4.2-18 Integrated S-band LHCP 2D Pattern (Phi = 0°, 90°) at 2200 MHz.....	47
4.2-19 Integrated S-band LHCP 2D Pattern (Phi = 0°, 90°) at 2350 MHz.....	47
4.2-20 Integrated S-band LHCP 2D Pattern (Phi = 0°, 90°) at 2500 MHz.....	48
4.3-1 Phase Center Alignment .....	51
4-4-1 Aperture Efficiency Vs. Reflector Half-angle and Focal/Diameter Ratio .....	53
4.4-2 S-band Horn and Ideal N=2 Feed Patterns and Aperture Efficiency .....	54
4.4-3 S-Band and X-band Aperture Efficiency (Mid-band) Vs. F/D .....	55
4.4-4 Aperture Efficiency and 2-D Pattern, X-band, RHCP, 8400 MHz .....	56
4.4-5 Aperture Efficiency and 2-D Pattern, X-band, RHCP, 8450 MHz .....	56
4.4-6 Aperture Efficiency and 2-D Pattern, X-band, RHCP, 8500 MHz .....	57
4.4-7 Aperture Efficiency and 2-D Pattern, X-band, LHCP, 8400 MHz.....	57
4.4-8 Aperture Efficiency and 2-D Pattern, X-band, LHCP, 8450 MHz.....	58

Figure	Page
4.4-9 Aperture Efficiency and 2-D Pattern, X-band, LHCP, 8450 MHz.....	58
4.4-10 Aperture Efficiency and 2-D Pattern, S-band, RHCP, 2200 MHz.....	59
4.4-11 Aperture Efficiency and 2-D Pattern, S-band, RHCP, 2350 MHz.....	59
4.4-12 Aperture Efficiency and 2-D Pattern, S-band, RHCP, 2440 MHz.....	60
4.4-13 Aperture Efficiency and 2-D Pattern, S-band, LHCP, 2200 MHz.....	60
4.4-14 Aperture Efficiency and 2-D Pattern, S-band, LHCP, 2350 MHz.....	61
4.4-15 Aperture Efficiency and 2-D Pattern, S-band, LHCP, 2440 MHz.....	61
4.5-1 Conceptual Dual Polarized OMT Feed Proposed by Hassan, et al.....	62

## LIST OF EQUATIONS

Equation	Page
Eq. 3.1-1.....	14
Eq. 3.1-2.....	14
Eq. 3.1-3.....	14
Eq. 3.1-4.....	14
Eq. 3.2-1.....	15

# CHAPTER 1

## INTRODUCTION

### 1.1 Linear Polarization

Linear polarization is defined as polarization of an electromagnetic wave in which the electric vector at a fixed point in space remains pointed in a fixed direction, although varying in magnitude (see Figure 1.1-1 Linear Polarization). There are two forms of linear polarization: vertical, where the electric field is perpendicular to the Earth's surface, and horizontal, where the electric field is parallel to the Earth's surface. Both directions can be used simultaneously on the same frequency. Some users of satellite systems consider linear polarization to be superior, if only because the specific equipment costs are marginally less as compared with circular polarization. Linear polarization can be found in both C- and Ku-Band (see Table 1.1-1 Polarization available on Intelsat satellites).

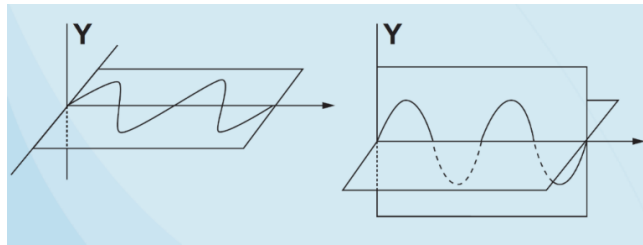


Figure 1.1-1 Linear Polarization

Circular Polarization:	
C-Band	IS-601, IS-602, IS-603, IS-605, IS-701, IS-702, IS-704, IS-705, IS-706, IS-707, IS-709, IS-801, IS-802, IS-901, IS-902, IS-903, IS-904, IS-905, IS-906, IS-907, IS-10-02
Ku-Band	None
Linear Polarization:	
C-Band	G-3C, G-4R, G-9, G-10R, G-11, G-12, G-13, G-14, G-15, G-16, G-23, G-25, G-26, G-27, G-28, Horizons 1, APR-1, IS-1R, IS-2, IS-3R, IS-5, IS-6B, IS-7, IS-8, IS-805, IS-9, IS-10 and IS-12
Ku-Band	All Satellites

## Table 1.1-1 Polarization available on Intelsat satellites

### 1.2 Circular Polarization

The benefits of increased reliability in signal strength, resistance to weather conditions, and ease of installation outweigh the marginally increased expense of the circularly polarized feed horn. Circular polarization (see Figure 1.2-1 Circular Polarization) involves the plane of polarization rotating in a corkscrew pattern, making one complete revolution during each wavelength. The circularly polarized wave will radiate energy in the horizontal and vertical plane, as well as every plane in between. There are two directions of propagation that come with circular polarization: Right-Hand-Circular (RHC) which follows a clockwise pattern, and Left-Hand-Circular (LHC) which follows a counterclockwise pattern. As with linear polarization, both directions can be used simultaneously on the same frequency, allowing higher revenue generation through the doubling of capacity on the satellites. Circular polarization can be found on both C-Band and Ku-Band (Intelsat being a notable exception, without any Ku-Band fleet with circular polarization, see Table 1.1-1 Polarization available on Intelsat satellites). This is because Ku-Band is at a high enough frequency that Faraday's effect is not a significant factor (see Section 1.4.1).

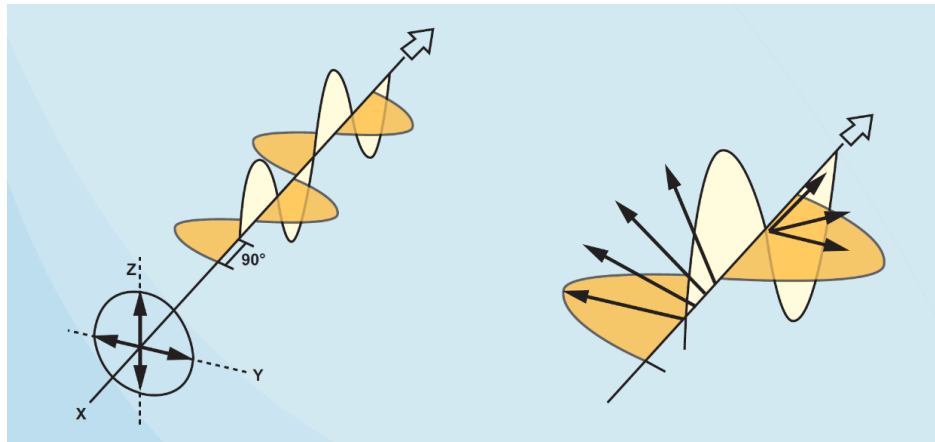


Figure 1.2-1 Circular Polarization

### 1.3 Circular Polarized Feed Horns

Switching from linear polarization to circular polarization is easier than many may think; it simply requires changing the feed horn that is mounted at the antenna's focal point. The price difference can be almost negligible. For example, a low cost VSAT antenna with two port feeds is a mere \$200 more than a linear feed horn. However, in some cases, the feed horn can be significantly more expensive for circular polarization, an investment which will be at least partially offset by its advantages.

Operationally, the feed horn conveys radio waves between the transceiver and the reflector. The feed horn also separates the two polarities (vertical from horizontal or left from right hand) of the signal being received. This removes unwanted signals, (for example, left hand circular), from the desired signal, (for example, right hand circular) of a given frequency. For a linear polarized feed horn to properly separate the polarizations, it must be precisely rotated to the exact alignment with the satellite's signals. A circular polarized feed horn does not have this requirement.





## 1.4 Advantages of Circular Polarization in Satellite Communications

There are several key advantages for circular polarization over linear polarization, which make it more appealing [1].

### 1.4.1 The Faraday Effect

The Faraday Effect (see Figure 1.4.1-1 Faraday's Effect: The Linear Polarized Signal Twists) deals with the interaction between light and magnetic fields. It affects linear, but not circular, polarized signals, and the effects are more severe at lower frequencies, such as C-Band (4/6 GHz), and not noticeable at higher ones, such as Ku-Band (11/14 GHz). As signals pass through the atmosphere, they become de-polarized, causing undesirable reception of the opposing polarity. Linear polarized feeds are aligned in such a way to compensate for the Faraday effect, usually with the help of a tracking device; corrections can be made either by rotating the feed system or using adjustable polarizers within the feed system. This can be very time consuming because the alignment must be exact.

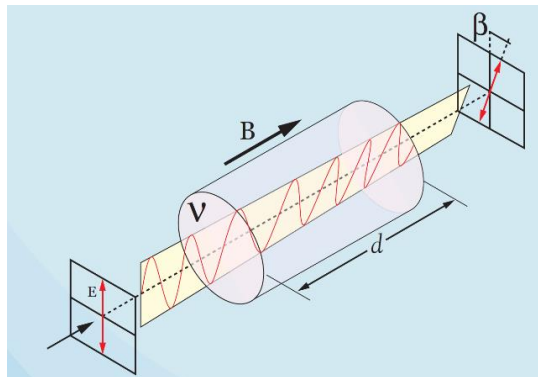


Figure 1.4.1-1 Faraday's Effect: The Linear Polarized Signal Twists

One result of incorrect alignment is increased interference. Fortunately, this is not a concern for circular polarization since there is no need for exact signal alignment. Ku-Band is at a high enough frequency that Faraday's effect is not a factor.

#### 1.4.2 Atmospheric Conditions

Circular polarization is more resistant to signal degradation due to atmospheric conditions. These conditions can cause changes in the rotation of the signal, and will more adversely affect linear polarization than circular polarization. The effect of a high frequency signal passing through rain can cause signal attenuation and accounts for the majority of the problems with rain fade. Moisture laden clouds are also a factor; by the time a signal passes through a cloud system it can be attenuated by as much as 1dB. Water droplets on the feed horn may also cause detrimental effects. However, the most important aspect to note is that higher frequencies (like Ku-Band) degrade faster, harder, and longer than their frequency counterparts (C-Band).

#### 1.4.3 Easier installation

The only requirement is ensuring that the antenna is aimed in the correct direction on the satellite; simply point and transmit. This allows for circular feeds to be set up quicker, and there is less of a risk of being misaligned.

#### 1.4.4 Higher link reliability

There is higher link reliability since there is a low risk of misalignment, and encountering interference. Faraday's effect will not affect transmission with circular C-band, so there will be no need to readjust the alignment. Finally, because transmission is sent and/or received at different frequencies, interference (cross polarization) is less of a concern.

## CHAPTER 2

### THEORETICAL BACKGROUND

#### 2.1 Linear to Circular Polarizer

Regardless of the specific implementation, a coax-fed circular polarizer converts the TEM mode coming in on one of the two orthogonal coax connectors to LHCP, and converts the TEM mode coming in on the other orthogonal coax connector to RHCP (from the transmit point of view).

There are three common ways to convert the TEM coax mode to circular polarization: (1) external hybrid combiner and orthogonal probes in a circular or square waveguide; (2) converting each TEM coax mode to the  $TE_{10}$  mode of a rectangular waveguide and then using a septum waveguide polarizer to convert one of the  $TE_{10}$  modes of the rectangular waveguide to LHCP in a square waveguide and the other  $TE_{10}$  mode to RHCP in a square waveguide; or (3) using orthogonal probes in a circular waveguide together with “bumps” that are internal to the circular waveguide, an approach known as the “Spread-Squeeze” Waveguide Polarizer, which will be described in Section 0. The goal of this thesis is to design, model and simulate a polarizer/feed based on the “Spread-Squeeze” waveguide polarizer. The orthogonal LHCP and RHCP modes are commonly used in one of two ways: (1) polarization diversity in receive-only systems; or (2) a Tx/Rx system that is receiving on one CP and transmitting on the orthogonal CP.

## 2.2 Commercial versions for comparison

Commercial versions of a S/X Dual Band CP feed/polarizer exist, such as the one shown in [Figure 2.2-1](#) made by M2 Antenna Systems, Inc. Evident in the picture on the left is an external 3-dB hybrid to convert from linear to circular polarization and vice versa. The spread-squeeze polarizer presented in this thesis eliminates this bulky and lossy component.



**M2 Antenna Systems, Inc.**  
Model No: FGFD-2-SC-XC-1  
S/X Dual-Band Dish Feed

**SPECIFICATIONS:**

Model Number .....	FGFD-2-SC-XC-1
S-Band Frequency Coverage .....	1.95-3.05 GHz (Customer Specific)
X-Band Frequency Coverage .....	7.0-8.5 GHz (Customer Specific)
Optimum Dish Feed F/D Ratio .....	0.3 TO 0.45
System Efficiency .....	50 TO 65%
Isolation Between Ports (S-Band) .....	>15 dB
Isolation Between Ports (X-Band) .....	>20 dB
Polarity .....	RHCP / LHCP
Connector .....	Type "N" Connector (WR-112 Flange Optional)
Dimensions .....	18" x 11.5" x 11.5"
Weight .....	14.5 lbs.

**FEATURES:**

The **M2 Antenna Systems, Inc.** FGFD-2-SC-XC-1. Dual-Band feed is designed for either Prime-Focus or Compact Cassegrain configured reflectors. The Dual-Circular S-Band section can support power levels in excess of 100 Watts for transmit applications. Band coverage in S-Band is from 1.5-3.05 GHz (Customer Specific), using precision "N" interface connections. The Dual-Circular X-Band section can support power levels in excess of 1 kW for transmit applications and covers the 7.0-8.5 GHz (Customer Specific) frequency range. The interface for X-Band is via the industry standard WR-112 waveguide flanges.

Using proprietary Frequency-Selective Surface (FFS) designs, **M2 Antenna Systems, Inc.** can fit multiple feeds on beam, increasing the capabilities of new or legacy reflectors. If your project is pressed for time, The M2 Engineering staff is ready to assist in sourcing, selection and design of the RF front end electronics, LNA's, LNB's, BUC's, Amplifiers, RF Cabling and referencing. Give us a call with your requirements today...we can help.

**M2 Antenna Systems, Inc. 4402 N. Selland Ave. Fresno, CA 93722**  
Tel: (559) 432-8873 Fax: (559) 432-3059 Web: [www.m2inc.com](http://www.m2inc.com)  
©2020 M2 Antenna Systems Incorporated

0406/2020  
Rev.01

Figure 2.2-1 Commercial S/X Dual-Band Feed using external hybrid combiner

The spec sheet shown in Figure 2.2-1 Commercial S/X Dual-Band Feed using external hybrid combiner for this commercial unit indicates that the frequency coverage requirements are Customer Specific. In the case of the spread-squeeze polarizer presented in this thesis, the objective is to illuminate a 3-meter satellite ground station parabolic dish having a focal length to diameter (F/D) ratio of 0.3. while achieving the best possible aperture efficiency, where aperture efficiency is defined as the ratio of the effective radiating area to the physical area of the aperture.

### 2.3 Spread-Squeeze Waveguide Polarizer

The Spread-Squeeze waveguide polarizer [2] [3] is a technique to convert linear polarization to circular polarization in a circular waveguide using “bumps” as in the crude sketch shown in Figure 2.3-1 Spread-Squeeze Polarizer conceptual diagram.

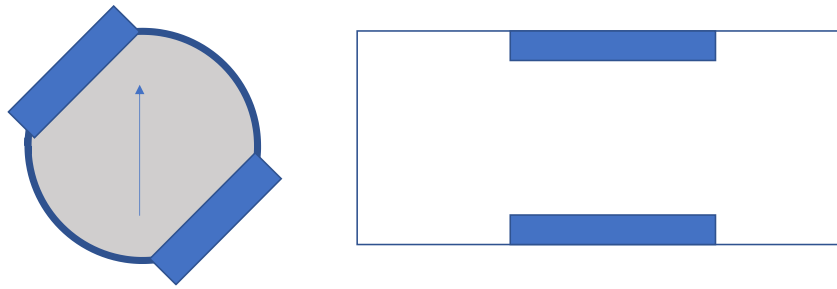
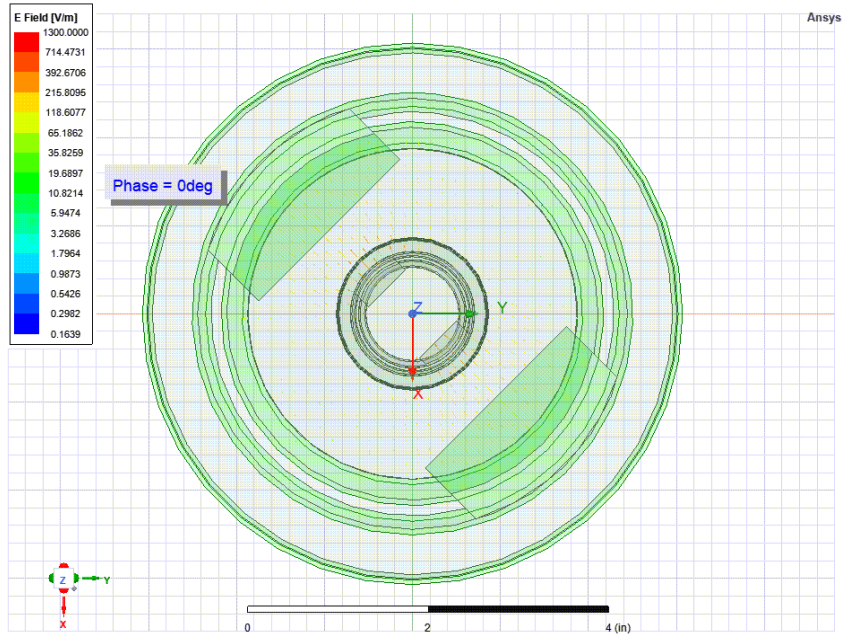
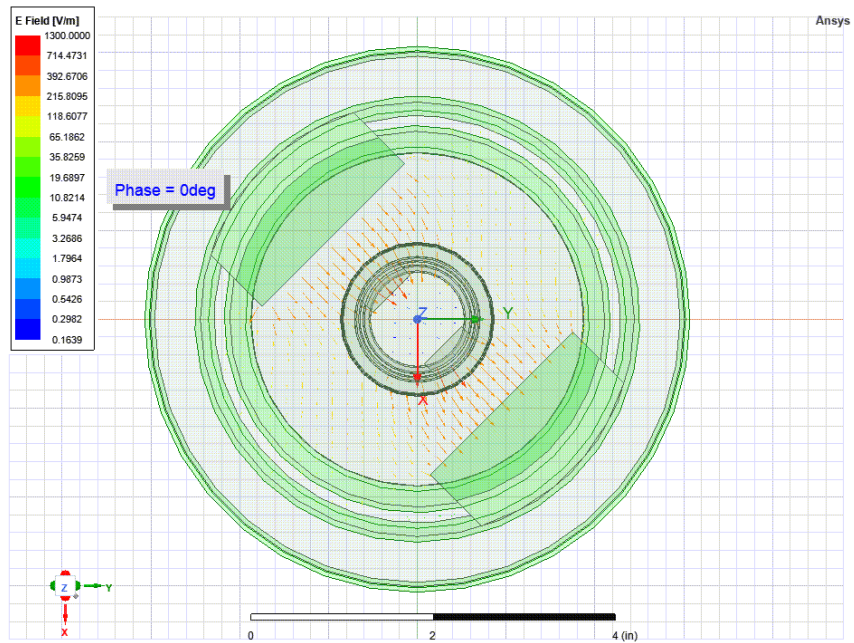


Figure 2.3-1 Spread-Squeeze Polarizer conceptual diagram

The basic idea is to put metal inserts approximately one-quarter wavelength long at 45 degrees to the orientation of the linear polarization, which results in a 90-degree phase shift. In the sketch, we can think of the “bumps” as converting vertical polarization to, say, RHCP. The same structure would then convert horizontal polarization to LHCP, and vice versa, so that incoming RHCP and LHCP are received by vertical and horizontal probes respectively. As shown in Figure 2.3-2 Conversion from linear  $TE_{11}$  to circular  $TE_{11}(v) \pm j TE_{11}(h)$ , (a) the TEM mode from the coax excites the linear  $TE_{11}$  mode in the circular waveguide, and (b) the spread-squeeze polarizer converts this to  $TE_{11}(v) \pm j TE_{11}(h)$ .



(a)  $TE_{11}$  in Circular Waveguide



(b)  $TE_{11}(v) \pm j TE_{11}(h)$

Figure 2.3-2 Conversion from linear  $TE_{11}$  to circular  $TE_{11}(v) \pm j TE_{11}(h)$



## CHAPTER 3

### DESIGN AND OPTIMIZATION

#### 3.1 Design Approach

The basic goals for the design in this paper are:

- S-band 2200 – 2450 MHz; X-band 8400 – 8500 MHz
- Antenna working frequencies:         S band,  $f_S = 2350 \pm 150$  MHz (12.8%)  
  X-band,  $f_X = 8450 \pm 50$  MHz (1.18%)
- Support RHCP & LHCP
- Minimize Axial Ratio (0 dB being perfect)
- Good port to port isolation (> 15 dB)
- Good radiation efficiency both bands (> 50% or better) – assume  $f/D$  ratio of 0.35
- Good input impedance,  $S_{11}$  (> 15 dB)

This design began with an existing reference design of a dual C/Ku band circular waveguide polarizer that uses the Spread-Squeeze approach. This dual-band design approach consists of two concentric waveguides, the higher frequency circular waveguide inside the lower frequency circular waveguide, with the higher frequency circular waveguide acting as a center conductor for the lower frequency band in a coaxial configuration. The higher frequency band signal propagates through the smaller diameter, inner cylinder functioning as a circular waveguide excited with its principle  $TE_{11}$  mode. The lower frequency band signal propagates through the space between the inner and outer cylinders functioning as a coaxial waveguide working above its cutoff TEM

frequency. See Figure 3.1-1 Dual-band coaxial waveguide dimensions. This configuration has the following important advantages [4]:

- both phase center positions lie almost in the same aperture plane for both bands
- excellent port to port isolation
- ease of assembly

The C/Ku dual-band reference design was scaled up in size for S-band and X-band, respectively. In addition, the geometry of the reference design was simplified to that of three vertically concatenated cones, with “bumps” intersecting (outer surfaces conforming to) the scaled geometry, and the walls thickened to 1/16<sup>th</sup> inch.

Adapting the reference design to our S/X dual-band application complies with the frequency spacing condition  $f_X \gg f_S$ . Coaxial waveguide radiation properties, cross-polarization suppression, size dependence etc., have been described by Olver et al. [5].

The schematic of the input waveguide for the dual S/X band design is shown in Figure 3.1-1 Dual-band coaxial waveguide dimensions. Both sections of the feed are excited with standard  $TE_{11}$  modes.

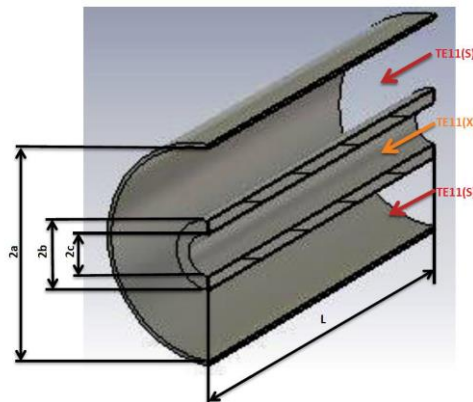


Figure 3.1-1 Dual-band coaxial waveguide dimensions

The inside diameter of the X-band waveguide,  $2c$ , in the design is 1.05904382 in (26.9 mm). Minimum and maximum frequencies for this cylindrical waveguide can be calculated from published formulae [4]. Critical frequencies for X-band TE<sub>11</sub> and approaching the higher mode TM<sub>01</sub> are:

$$f_{X_{TE11}} = 300/3.412c = 6.53 \text{ GHz} \quad \text{Eq. 3.1-1}$$

$$f_{X_{TM01}} = 300/2.613c = 8.54 \text{ GHz} \quad \text{Eq. 3.1-2}$$

The condition for single-mode operation is thus satisfied:  $f_{X_{TE11}} < f_X < f_{X_{TM01}}$

The wall thickness of the X-band waveguide was selected to be 1/16<sup>th</sup> inch (1.5875 mm). From this,  $b$  in Figure 3.1-1 Dual-band coaxial waveguide dimensions is calculated to be 15.0373565 mm.

The radius  $a$  in Figure 3.1-1 Dual-band coaxial waveguide dimensions is 1.874595 in. (47.61 mm).

Using these dimensions, we can calculate the basic S-band TE<sub>11</sub> mode frequency range [5]:

$$f_{S_{TE11}} = \frac{300}{1.873 \frac{\pi}{2} (a + b)} = 1.63 \text{ GHz} \quad \text{Eq. 3.1-3}$$

$$f_{S_{TE21}} = \frac{300}{1.023 \frac{\pi}{2} (a + b)} = 2.98 \text{ GHz} \quad \text{Eq. 3.1-4}$$

Again, the condition for single-mode operation is satisfied:  $f_{S_{TE11}} < f_S < f_{S_{TE21}}$

### 3.2 Port to Port Isolation [4]

Eq. 3.1-1 clearly demonstrates that the X-band waveguide functions as an effective attenuator, since for the S-band it acts as a waveguide below its critical frequency. The value of attenuation can be calculated using adapted formula (5) from [5]

$$ATT_{WG} = 0.1819 f X_{TE11} \sqrt{1 - \left(\frac{fS}{fX_{TE11}}\right)^2}, \text{ (dB/mm, GHz)} \quad \text{Eq. 3.2-1}$$

For our values  $f X_{TE11} = 6.53$  GHz and  $f S = 2.350$  GHz, theoretical waveguide attenuation  $ATT_{WG} = 1.11$  dB/mm. For 7 inches (178mm) the calculated isolation is 197 dB. In actual practice, RF connectors and cable leakage would reduce this to a value of about 100 dB, which is still very good.

### 3.3 Isolated X-, S-band Radiation Patterns and Input Impedance

The isolated X-band design is shown in Figure 3.3-1. The input waveguide and horn are aligned with and symmetric around the Z-axis. As noted above, the scaled geometry was simplified to facilitate the manufacturing process. The horn consists of three vertically concatenated cone sections and two annular rings at the base of the two upper cones that are closest to the aperture. The “bumps” in the design have four design parameters, which are independently optimized in each frequency band (not simply scaled). The input waveguide is extended 7 inches in length such that the waveport extends just beyond that of the S-band horn when integrated.

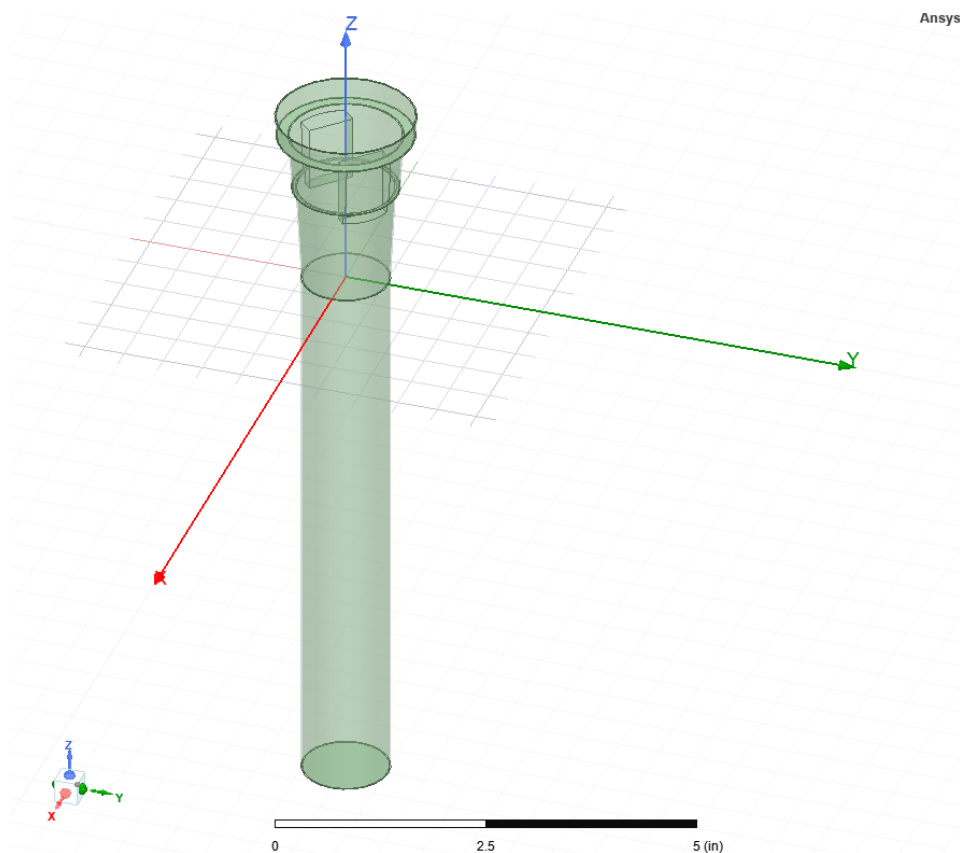


Figure 3.3-1 Isolated X-band design

The X-band isolated Realized Gain for RHCP is shown in Figure 3.3-2.

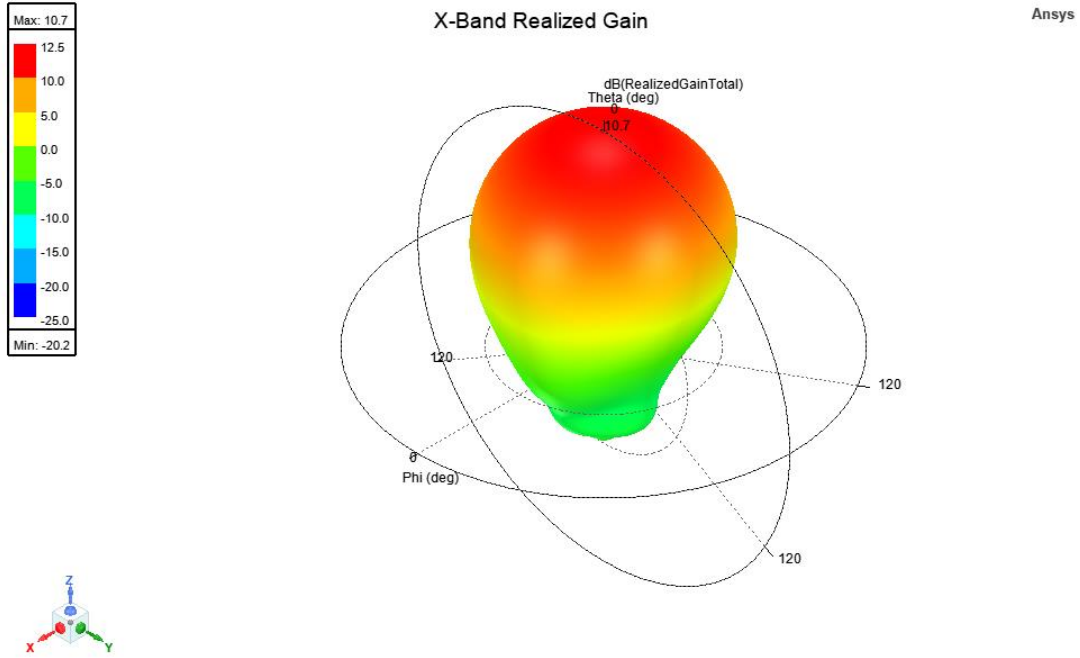


Figure 3.3-2. Calculated 3D X-band RHCP radiation pattern (8450 MHz)

The axial ratio for the isolated X-band horn is shown in Figure 3.3-3

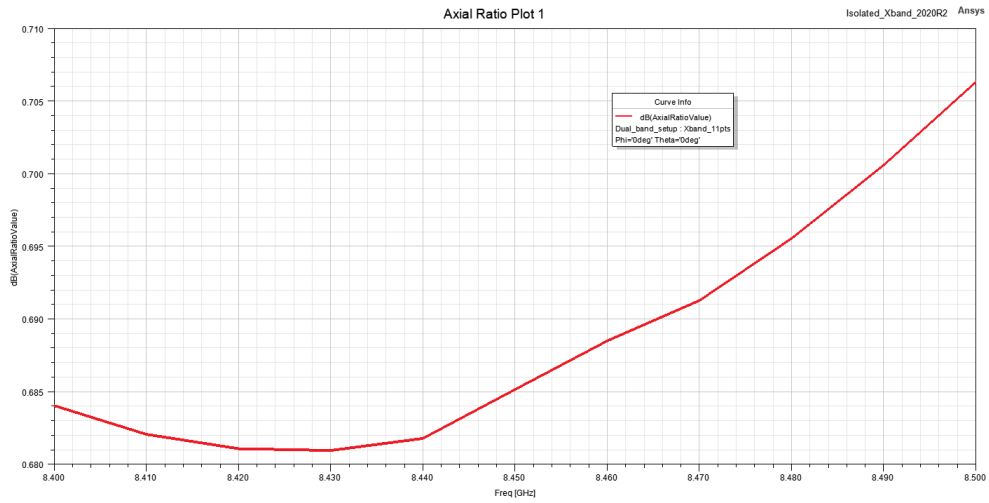


Figure 3.3-3 Axial ratio for isolated X-band horn ( $\phi = \theta = 0^\circ$ )

The input impedance for the isolated X-band horn is plotted in Figure 3.3-4.

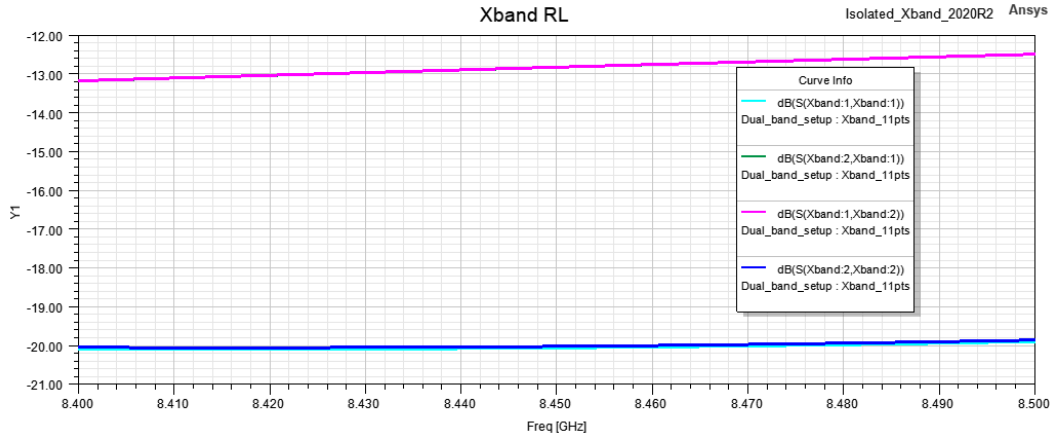


Figure 3.3-4 *S11* (mode1/mode2) calculated impedance match of the X-band port. The port employs a  $\lambda/4$  excitation probe, created from the center pin of a SMA connector.

Four probes are used to excite the S-band coaxial waveguide. Probes are fed with  $0^\circ$ ,  $90^\circ$ ,  $180^\circ$ , and  $270^\circ$  phase shift. This creates circular polarization. See Figure 3.3-5.

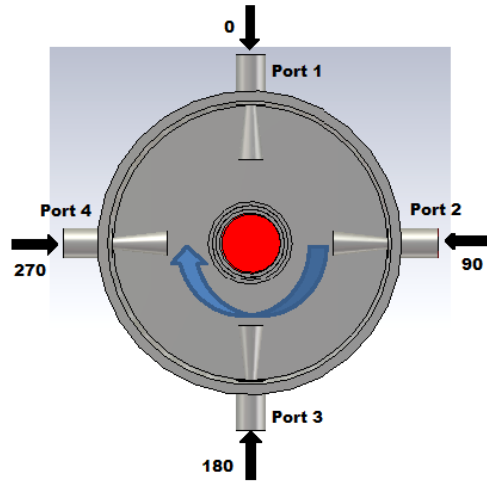


Figure 3.3-5 Feed boresight axis view. Four probes are fed with phase shifted signals exciting RHCP in this figure. To change the sense of rotation, excitation signals of two opposite ports must be exchanged.

The S-band HFSS model is shown in Figure 3.3-6

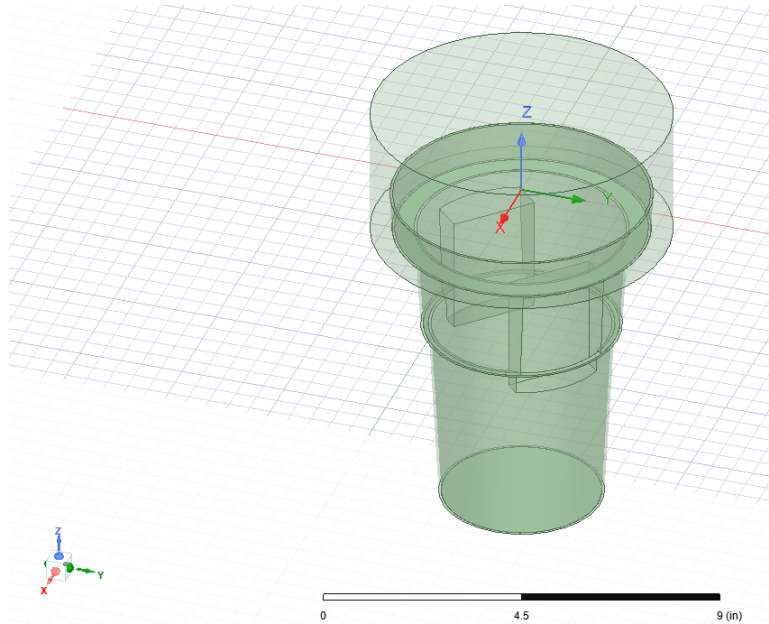


Figure 3.3-6 S-band horn modeled in HFSS

The simulated S-band radiation pattern and axial ratio are shown in Figures 3.3-7 and 3.3-8



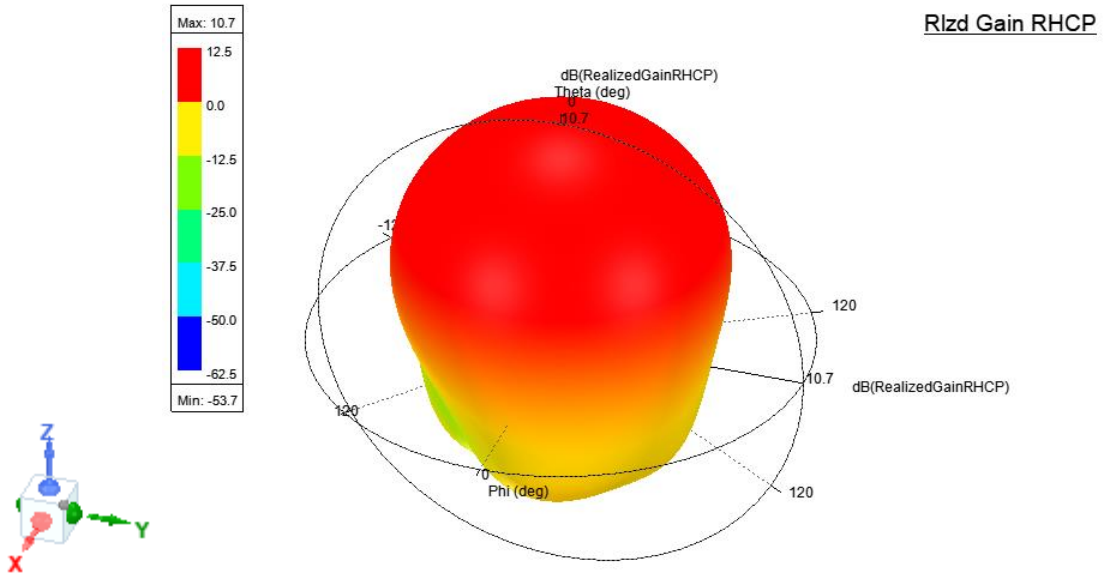


Figure 3.3-7 Calculated S-band 3D radiation pattern. RHCP is displayed.

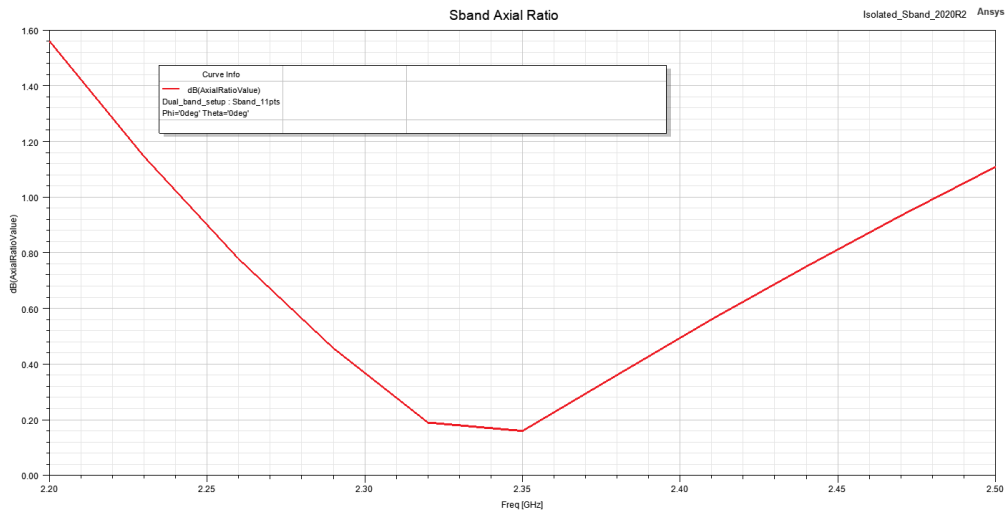


Figure 3.3-8 Calculated S-band axial ratio for  $\Phi = 0$  deg.

## CHAPTER 4

### FINAL RESULTS

In this chapter, the simulated performance of the integrated dual band horn feed is presented. The dual band horn feed is realized by combining the S-band and the X-band horn designs described in the previous chapters, aligning the phase centers, and optimizing the performance. Henceforth, the dual band horn feed is referred to as the “integrated design.”

#### 4.1 Integrated X-band Performance

The geometry of the integrated design as captured in Ansys HFSS is shown in Figures 4.1-1 and 4.1-2.

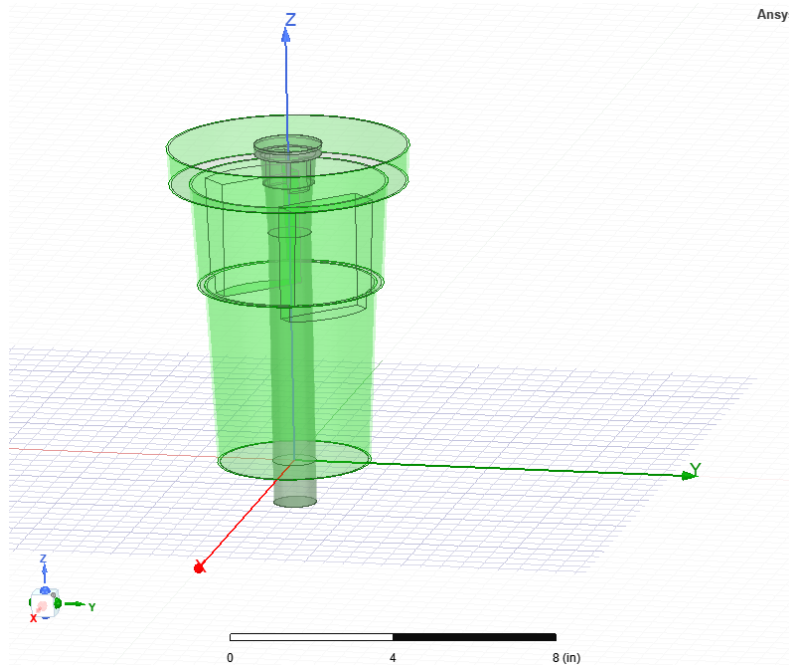
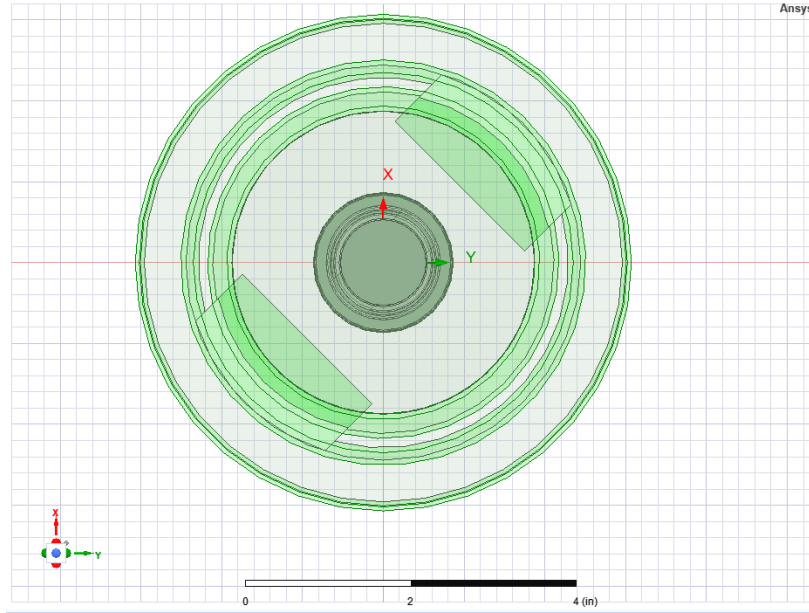
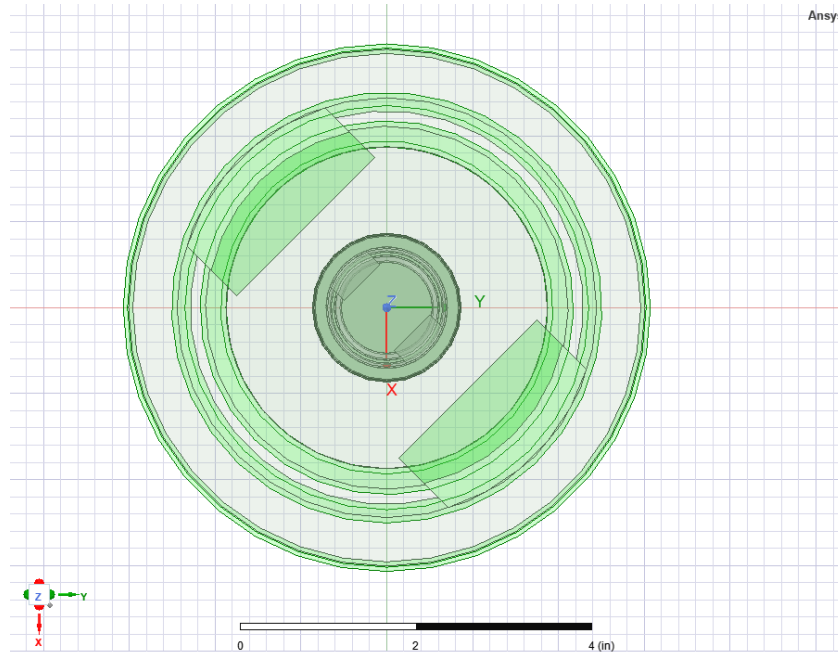


Figure 4.1-1 Integrated X-band and S-band horns (HFSS)



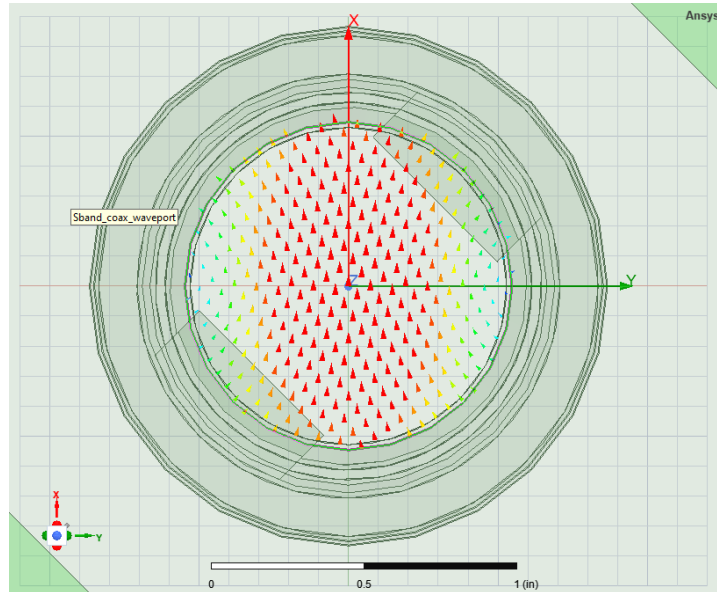
(a) Bottom view (looking into ports)



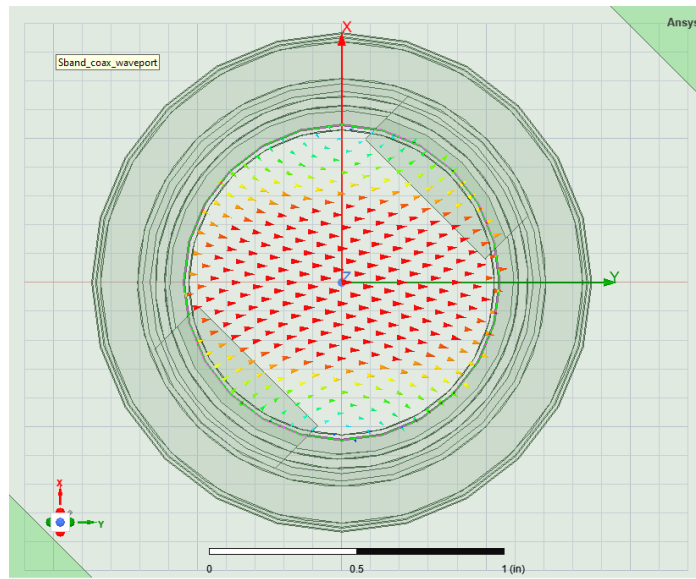
(b) Top view (looking into apertures)

Figure 4.1-2 Integrated S/X band horn (HFSS)

The X-band port fields are plotted in Figure 4.1-3, (a) Mode 1, and (b) Mode 2.

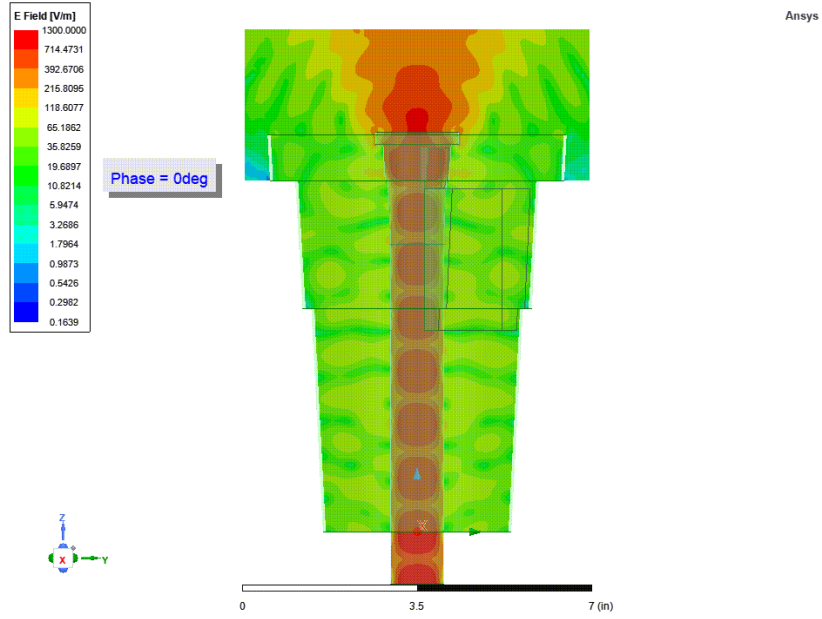


(a) X-band mode 1 (RHCP) port fields

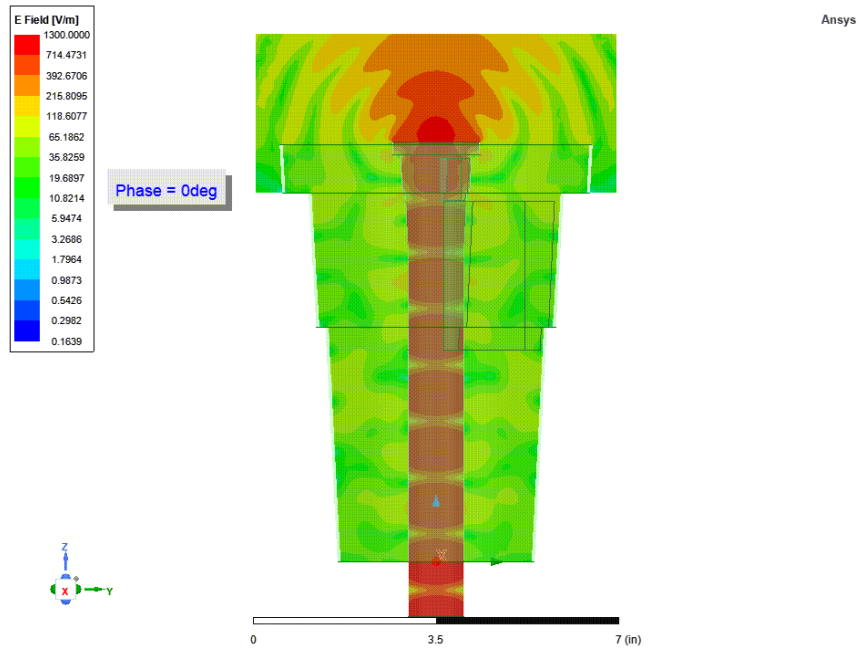


(b) X-band mode 2 (LHCP) port fields

Figure 4.1-3 X-band Mode 1 port fields



(a) Integrated X-band fields (mode1, RHCP)



(b) Integrated X-band fields (mode2, LHCP)

Figure 4.1-4 Integrated X-band longitudinal mag E fields

The X-band mode 1 axial ratio at boresight ( $\phi = \theta = 0^\circ$ ) across the desired passband (8400-8500 MHz) is plotted in Figure 4.1-5. The mode 2 axial ratio is plotted in Figure 4.1-6.

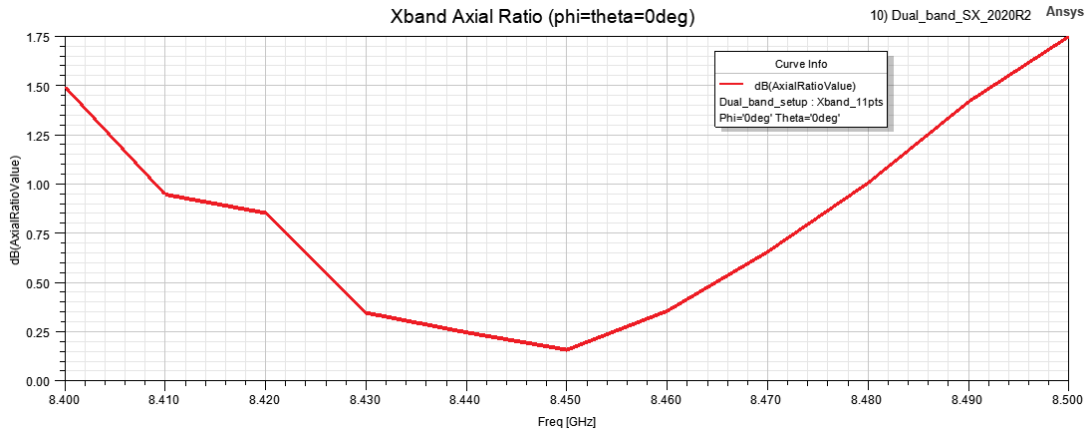


Figure 4.1-5 Integrated X-band Mode 1 axial ratio

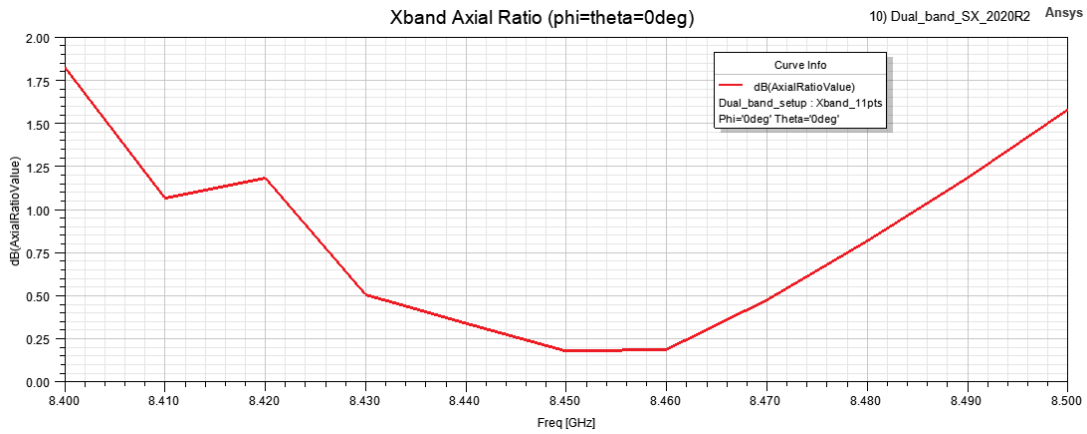


Figure 4.1-6 Integrated X-band Mode 2 axial ratio

The X-band RHCP 3D polar patterns ( $\phi = 0^\circ$ ) are plotted at low- (8400 MHz), mid- (8450 MHz), and high- (8500 MHz) band in Figures 4.1-7, 4.1-8, and 4.1-9, respectively.

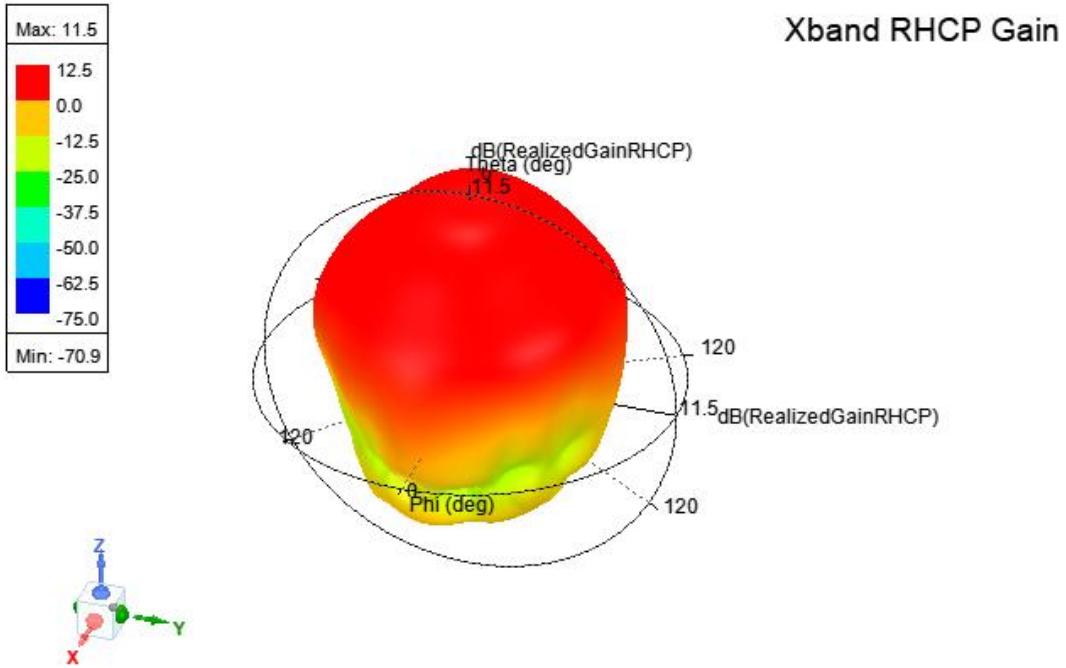


Figure 4.1-7 X-band 3D polar plot (RHCP, low-band, 8400 MHz)

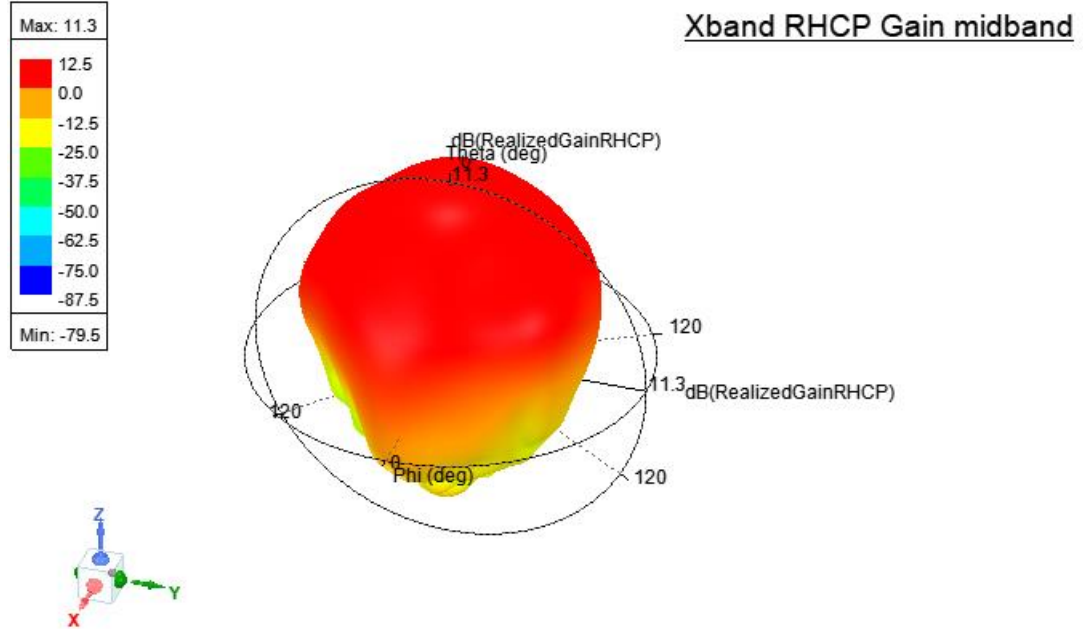


Figure 4.1-8 X-band 3D polar plot (RHCP, mid-band, 8450 MHz)

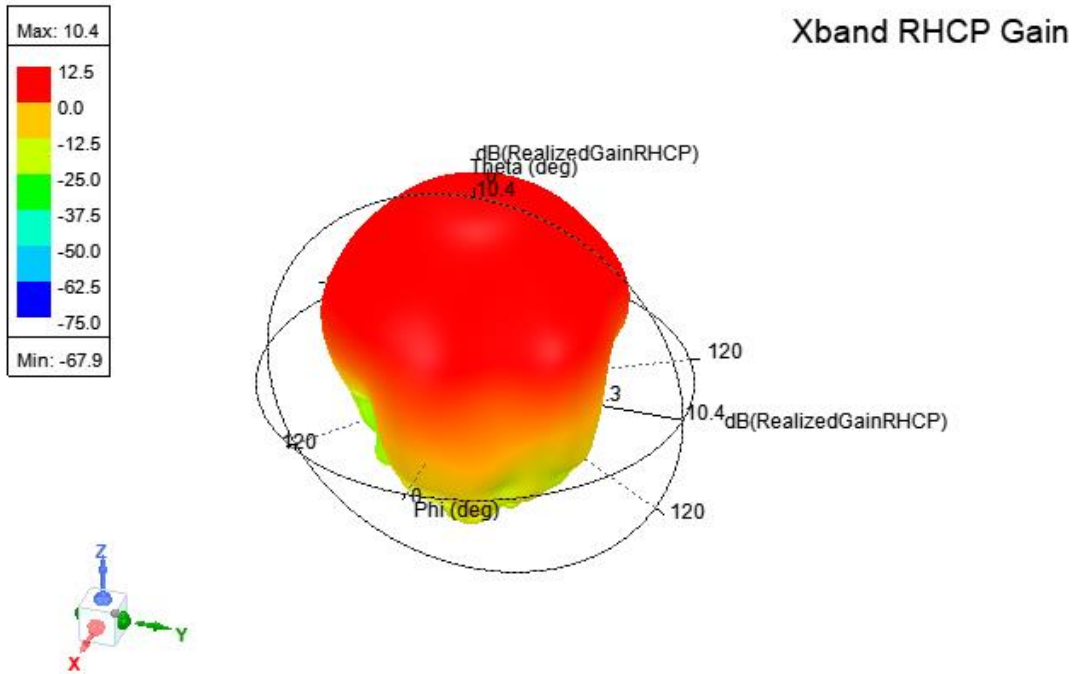


Figure 4.1-9 X-band 3D polar plot (RHCP, high-band, 8500 MHz)

The X-band LHCP 3D patterns are plotted in Figures 4.1-10, 4.1-11, and 4.1-12, respectively.



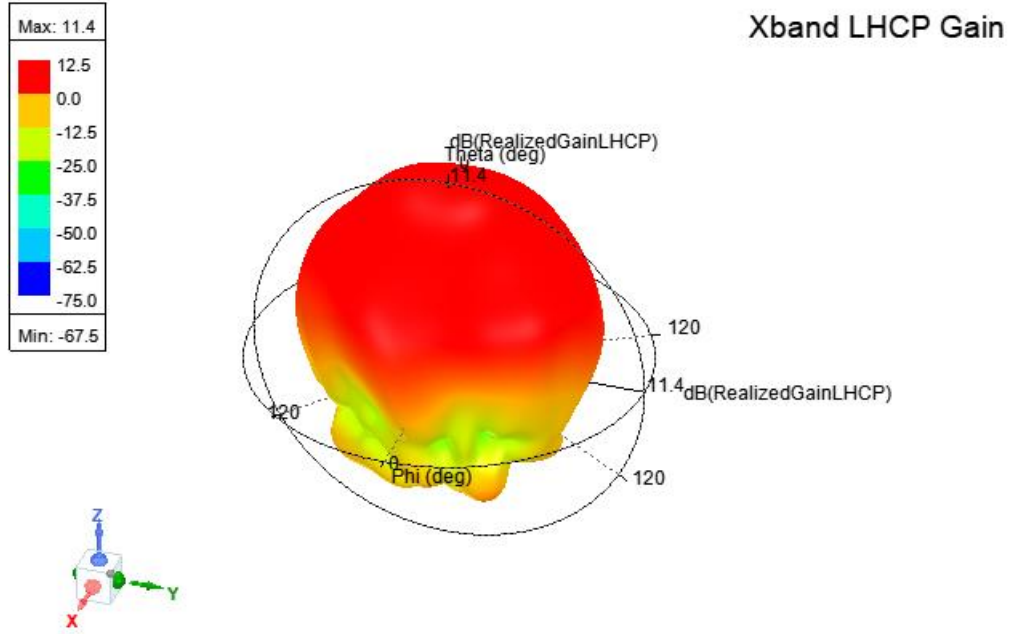


Figure 4.1-10 X-band 3D polar plot (LHCP, low-band, 8400 MHz)

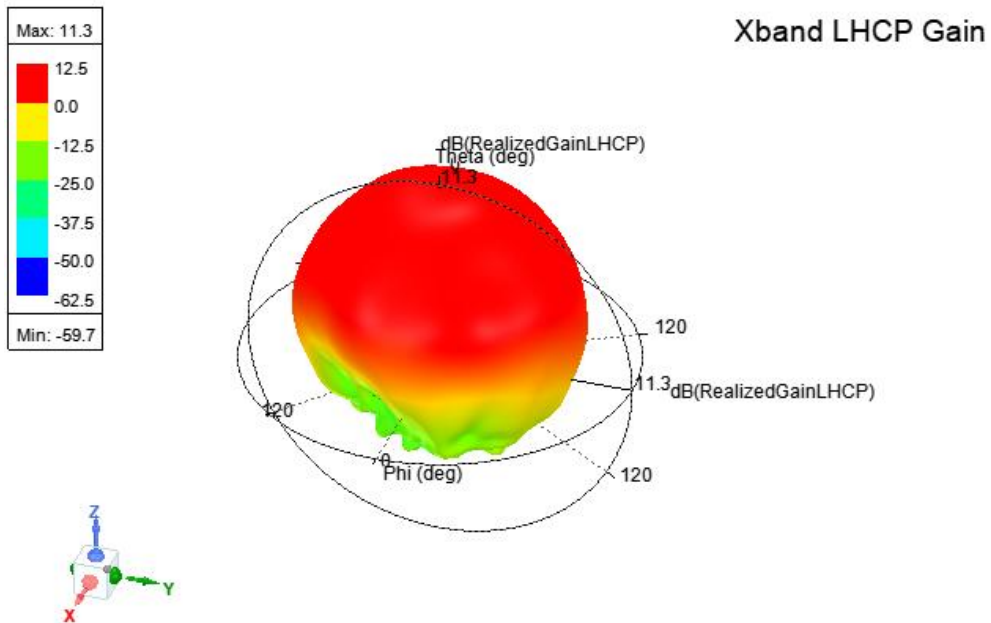


Figure 4.1-11 X-band 3D polar plot (LHCP, mid-band, 8450 MHz)

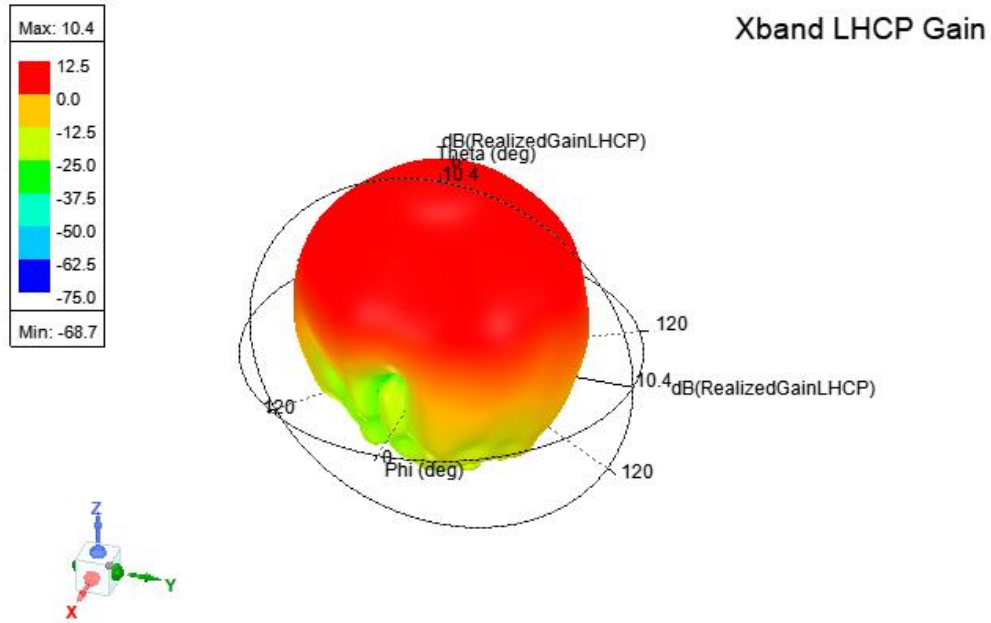


Figure 4.1-12 X-band 3D polar plot (LHCP, high-band, 8500 MHz)

The X-band horn RHCP 2D pattern cuts ( $\phi = 0^\circ, 90^\circ$ ) are plotted at low-, mid-, and high-band in Figures 4.1-13, 4.1-14, and 4.1-15, respectively, with the corresponding 3 dB (half-power) beamwidths.

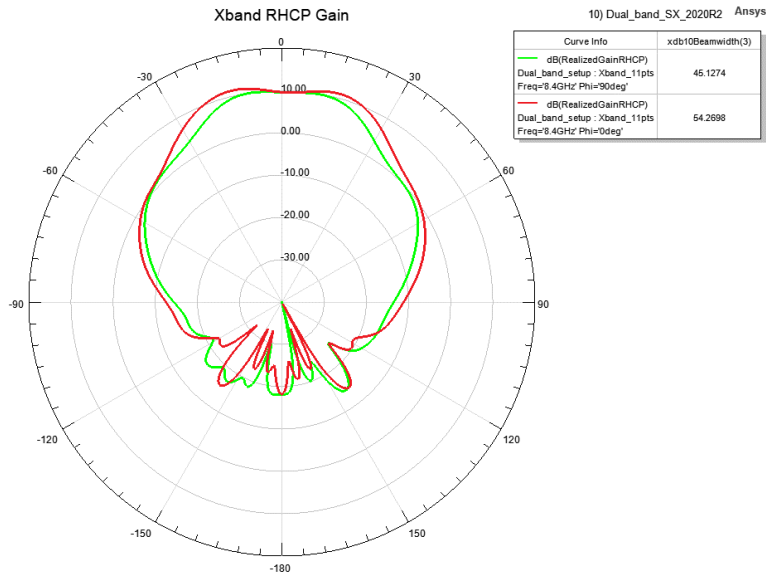


Figure 4.1-13. X-band RHCP 2-D radiation pattern ( $\phi = 0^\circ, 90^\circ, 8400 \text{ MHz}$ ) with table giving the corresponding 3dB beamwidths.

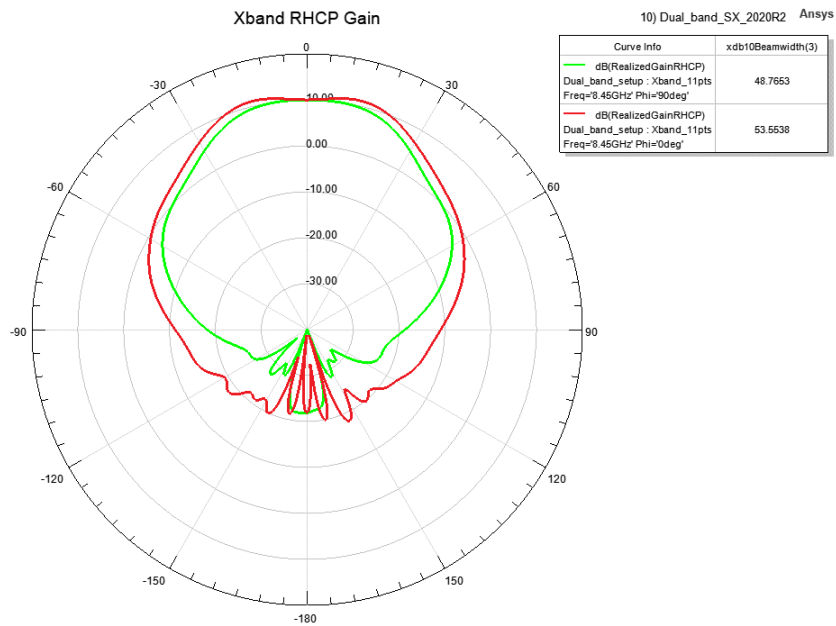


Figure 4.1-14 X-band RHCP 2-D radiation pattern ( $\phi = 0^\circ, 90^\circ, 8450 \text{ MHz}$ ) with table giving the corresponding 3dB beamwidths.

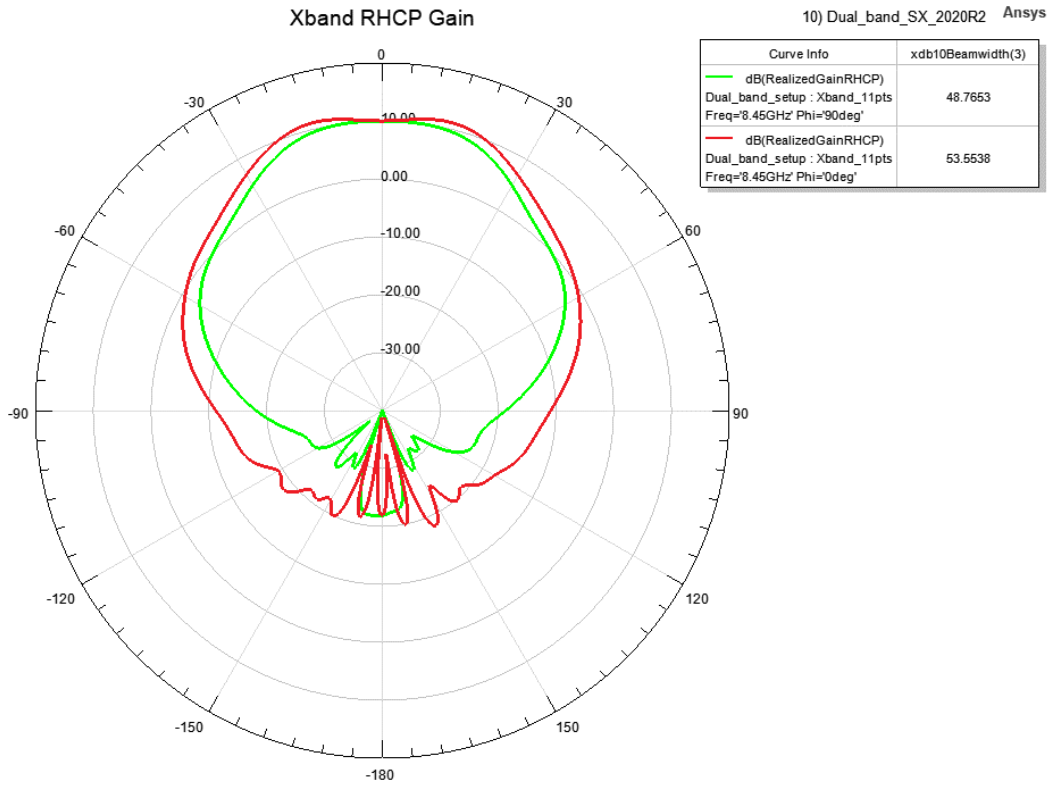


Figure 4.1-15 X-band RHCP 2-D radiation pattern ( $\phi = 0^\circ, 90^\circ, 8500 \text{ MHz}$ ) with table giving the corresponding 3dB beamwidths.

The X-band horn LHCP 2D pattern cuts ( $\phi = 0^\circ, 90^\circ$ ) are plotted at low-, mid-, and high-band in Figures 4.1-16, 4.1-17, and 4.1-18, respectively, with the corresponding 3 dB (half-power) beamwidths.

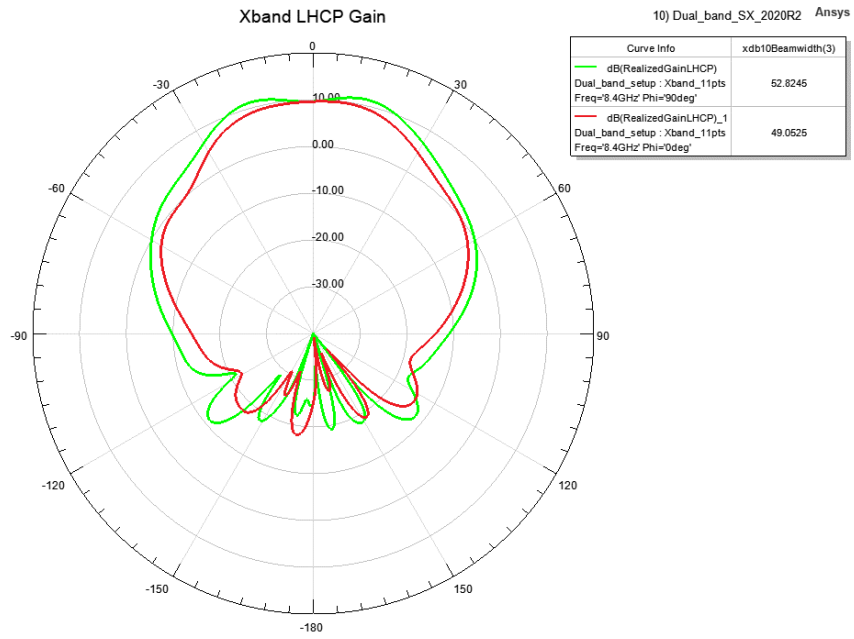


Figure 4.1-16 X-band LHCP 2-D radiation pattern ( $\phi = 0^\circ, 90^\circ, 8400 \text{ MHz}$ ) with table giving the corresponding 3dB beamwidths.

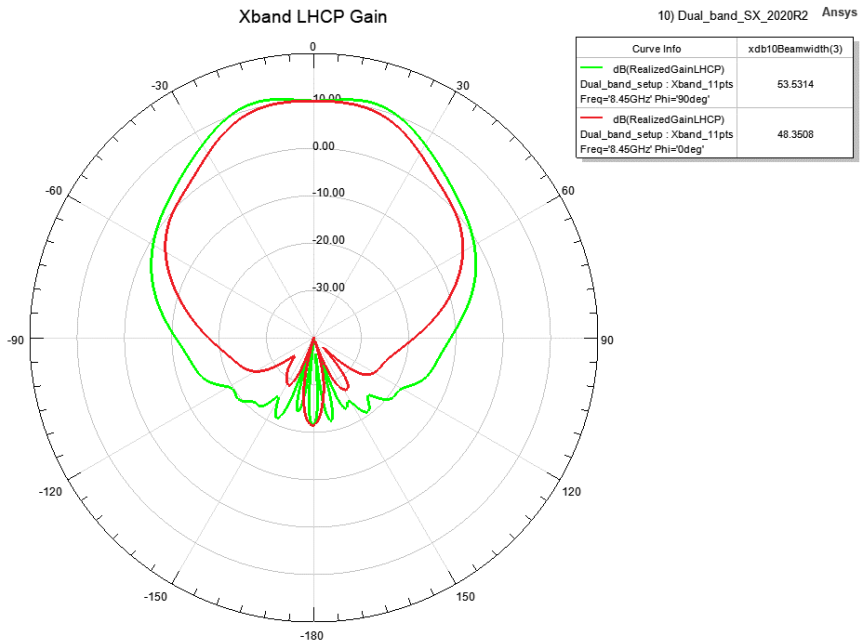


Figure 4.1-17 X-band LHCP 2-D radiation pattern ( $\phi = 0^\circ, 90^\circ, 8450 \text{ MHz}$ ) with table giving the corresponding 3dB beamwidths.

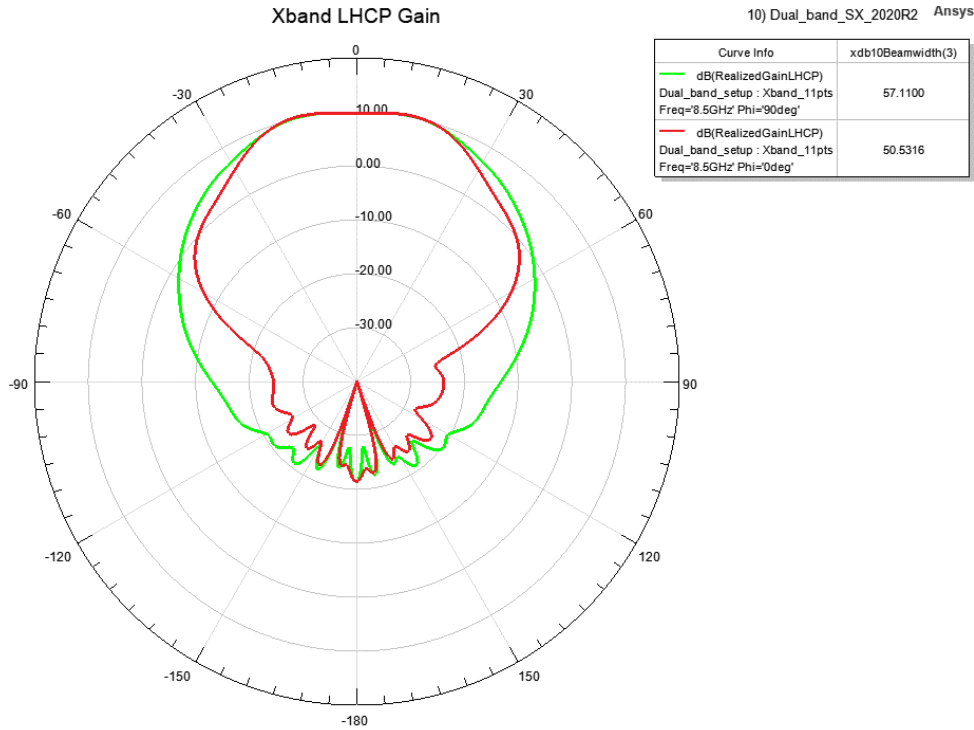


Figure 4.1-18 X-band LHCP 2-D radiation pattern ( $\phi = 0^\circ, 90^\circ, 8500 \text{ MHz}$ ) with table giving the corresponding 3dB beamwidths.

The input S-parameters with X-band Mode1 incident are plotted in Figure 4.1-19. The quantities  $S(\text{Xband\_wg\_waveport1}, \text{Xband\_wg\_waveport1})$  and is the input reflection coefficient for Mode1, and the quantity  $S(\text{Xband\_wg\_waveport2}, \text{Xband\_wg\_waveport1})$  is the isolation between Mode1 and Mode2.

The input S-parameters with X-band Mode2 incident are plotted in Figure 4.1-20. The quantity  $S(\text{Xband\_wg\_waveport2}, \text{Xband\_wg\_waveport2})$  is the input reflection coefficient for Mode2, and the quantity  $S(\text{Xband\_wg\_waveport1}, \text{Xband\_wg\_waveport2})$  is the isolation between Mode2 and Mode1.

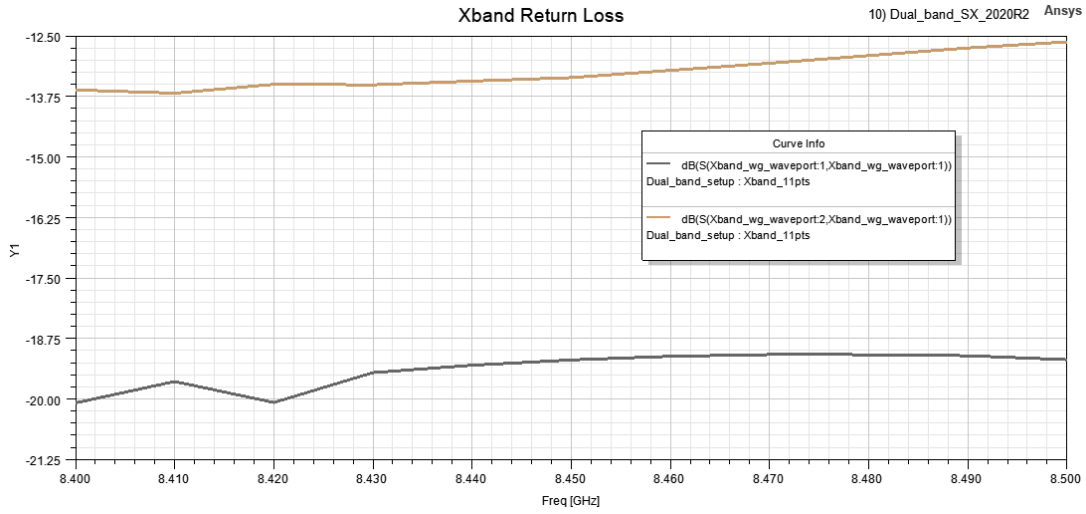


Figure 4.1-19 Integrated X-band Input Return Loss Mode1 incident

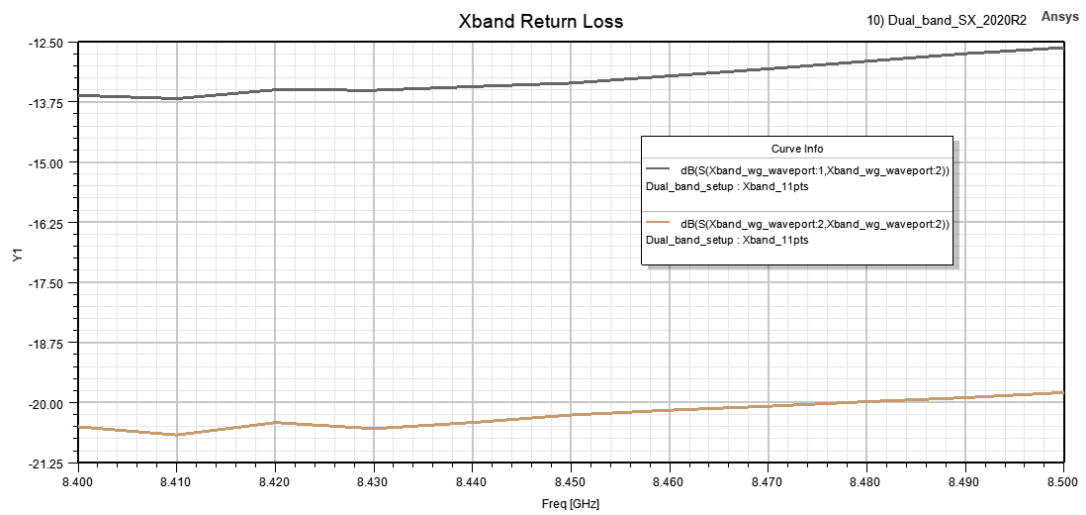


Figure 4.1-20 Integrated X-band Input Return Loss Mode2 incident

The isolation at S-band port2 and port3 due to X-band Mode1, Mode2 incident is plotted in Figure 4.1-21.

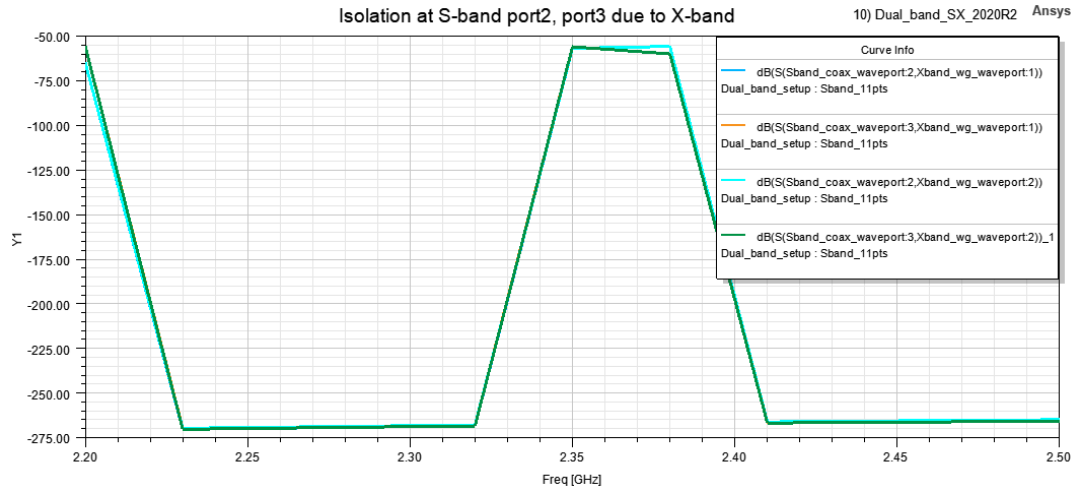
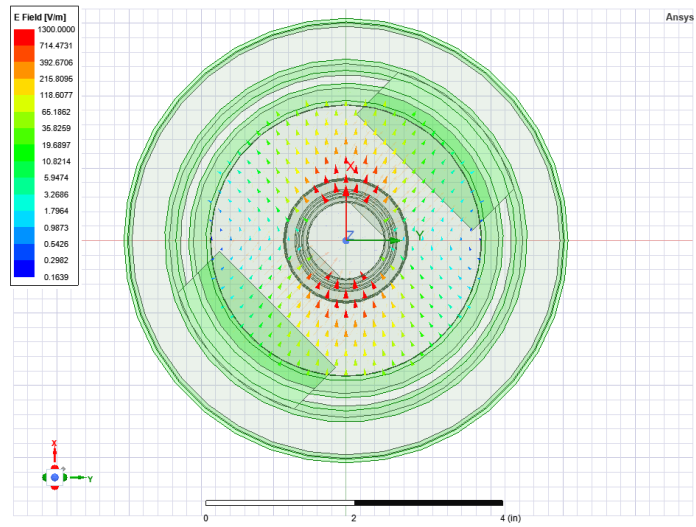


Figure 4.1-21 Isolation at S-band due to X-band Mode1, Mode2 incident

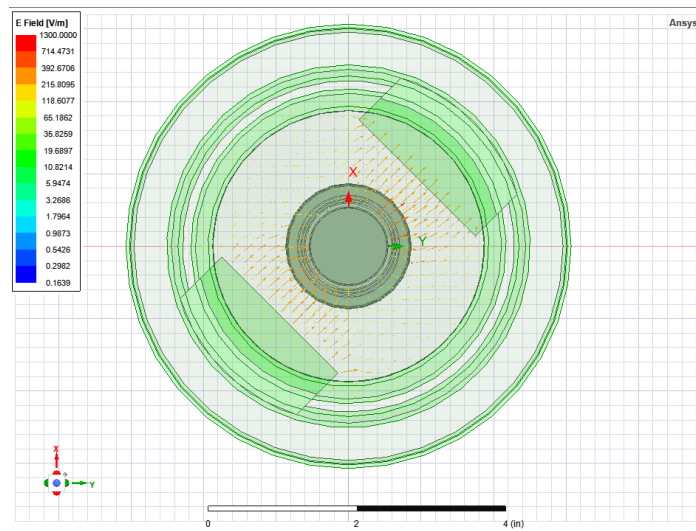


## 4.2 Integrated S-band Performance

The integrated S-band Mode1 port fields are shown in Figure 4.2-1(a) and the Mode2 port fields in Figure 4.2-1(b)

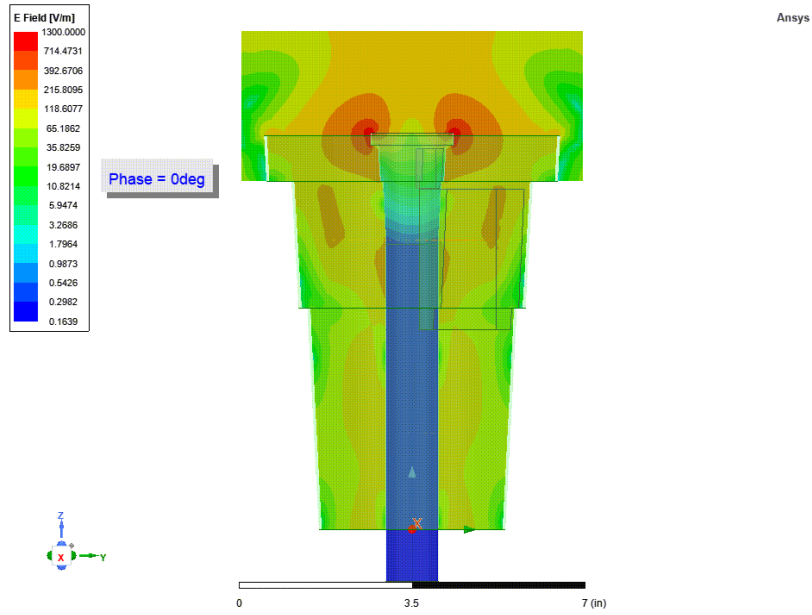


(a) Integrated S-band port fields Mode 1 (RHCP)

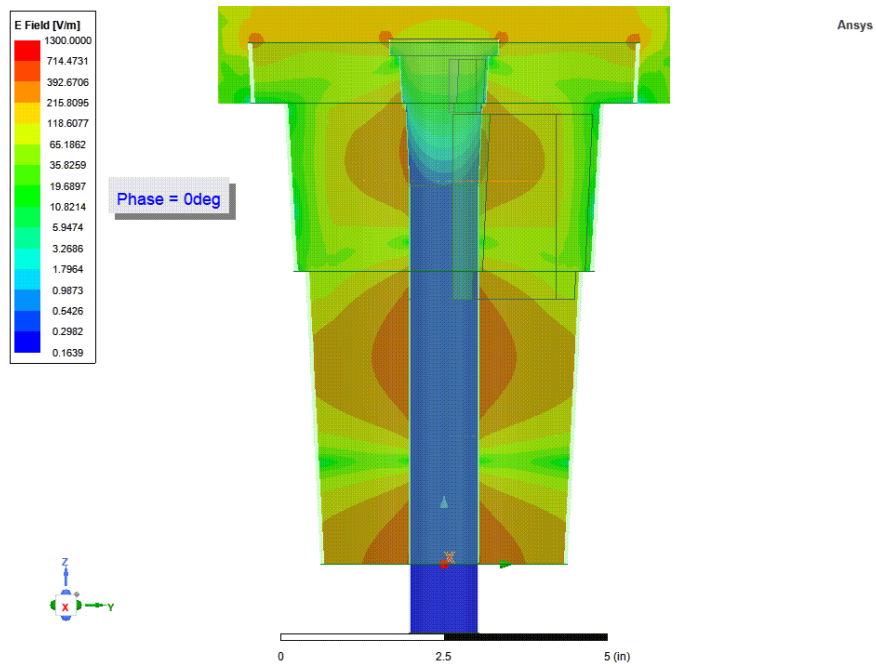


(b) Integrated S-band port fields Mode 2 (LHCP)

Figure 4.2-1 Integrated S-band port fields



(a) Integrated S-band Mode 1 (RHCP)



(b) Integrated S-band Mode 2 (LHCP)

Figure 4.2-2 Integrated S-band longitudinal mag E fields

The integrated S-band Mode1 axial ratio ( $\phi = \theta = 0^\circ$ ) is plotted in Figure 4.2-3.

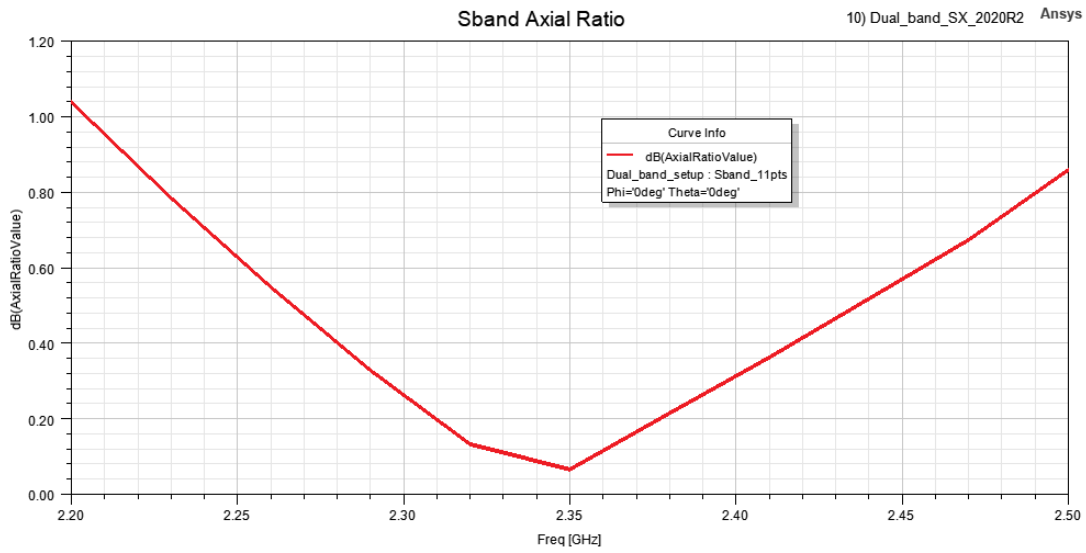


Figure 4.2-3 Integrated S-band axial ratio (mode1, TE<sub>11</sub>)

The integrated S-band Mode2 axial ratio ( $\phi = \theta = 0^\circ$ ) is plotted in Figure 4.2-4.

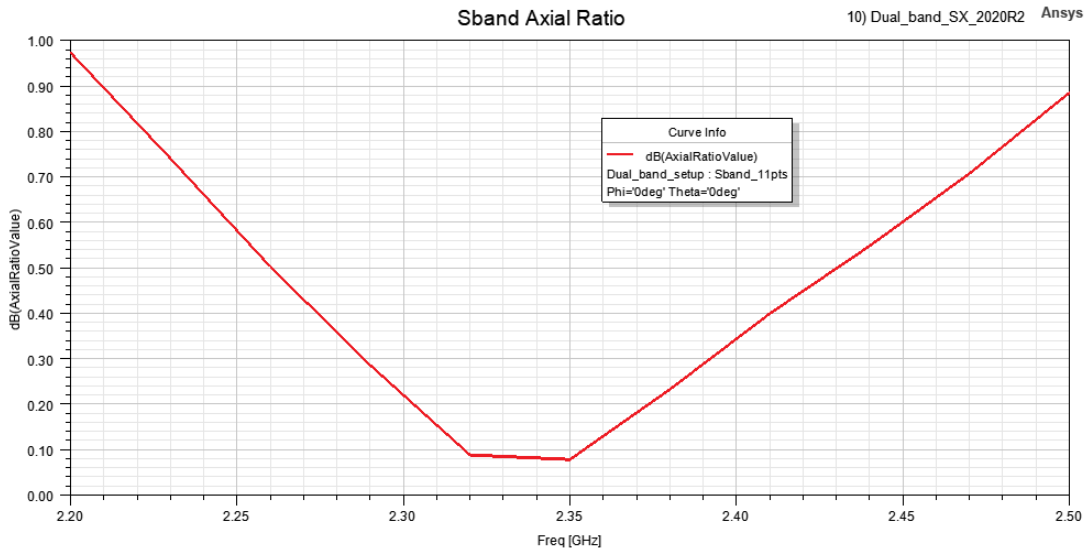


Figure 4.2-4 Integrated S-band Mode2, TE<sub>11</sub> axial ratio

The integrated S-band input return loss and isolation between the modes (Mode1 incident) is plotted in Figure 4.2-5. Note that Mode1 is port2, Mode2 is port3 (port1 is TEM not allowed).

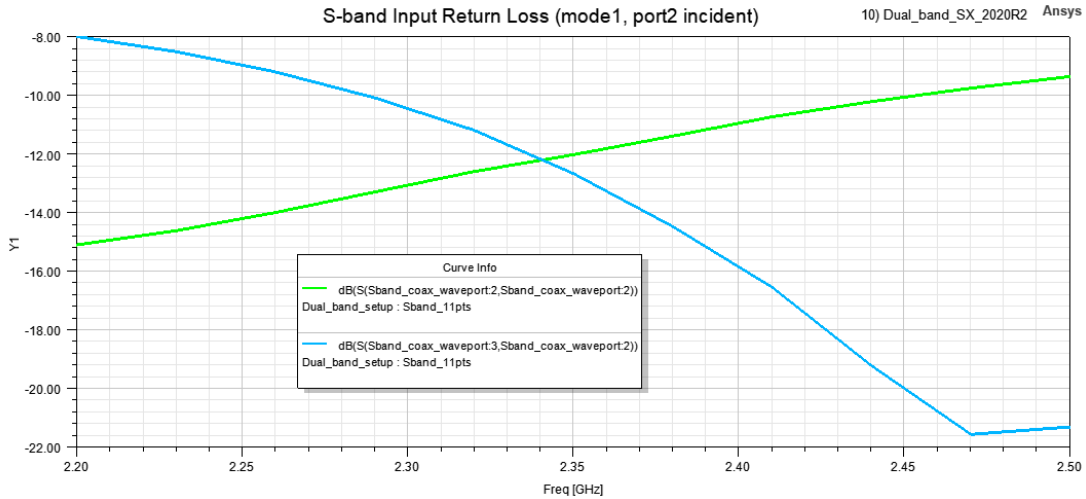


Figure 4.2-5 Integrated S-band input return loss (Mode1 incident)

The isolation at X-band port1, port2 due to S-band port2 (mode1) incident is plotted in Figure 4.2-6.

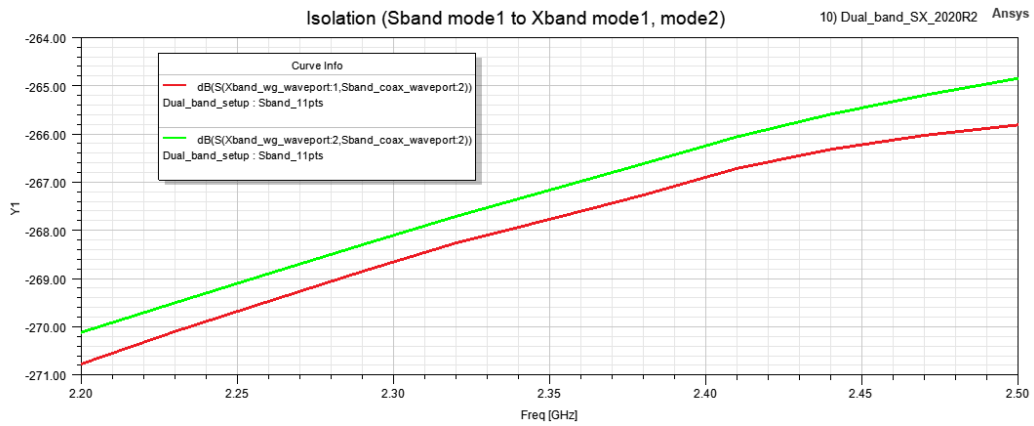


Figure 4.2-6 Isolation at X-band port1, port2 due to S-band port2 (mode1) incident

The integrated S-band input return loss and isolation between the modes (Mode2 incident) is plotted in Figure 4.2-7. Note that Mode1 is port2, Mode2 is port3 (port1 is TEM not allowed).

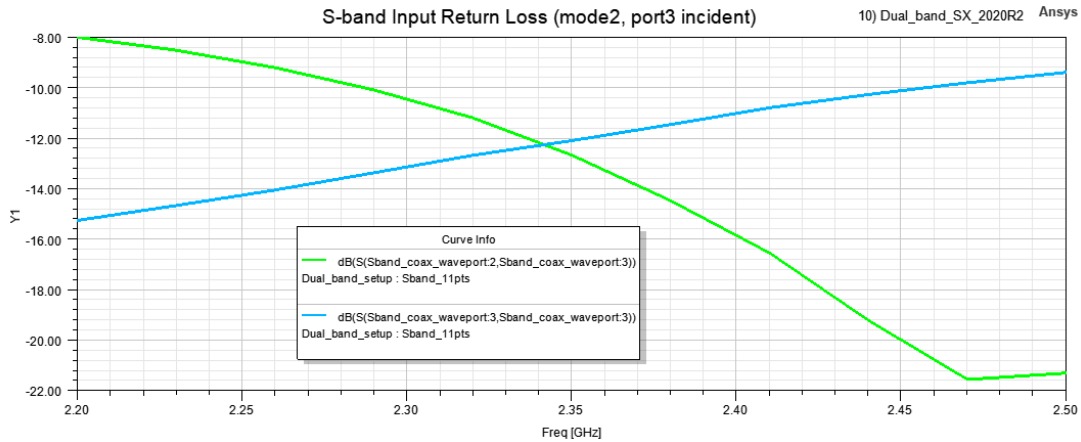


Figure 4.2-7 Integrated S-band input return loss (Mode2 incident)

The isolation at X-band port1, port2 due to S-band port3 (mode2) incident is plotted in Figure 4.2-8.

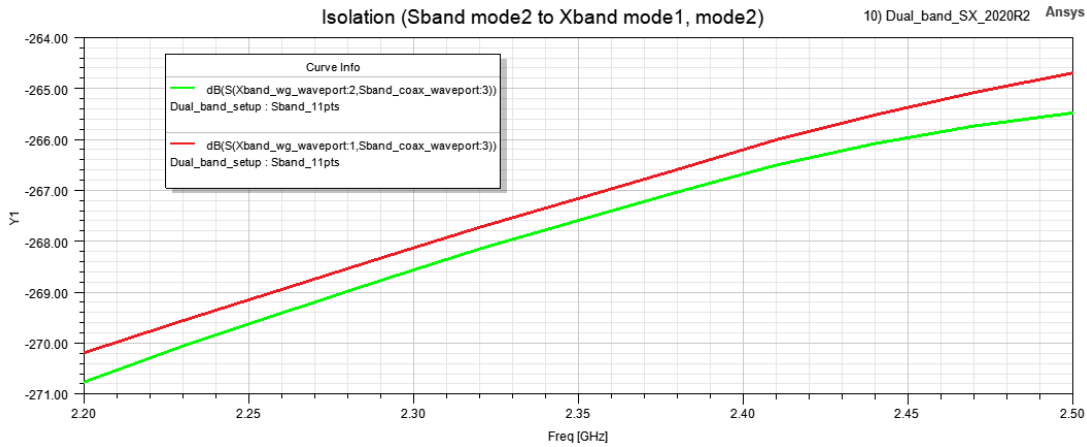


Figure 4.2-8 isolation at X-band port1, port2 due to S-band port3 (mode2) incident

The integrated S-band RHCP 3D polar radiation pattern for low-, mid-, and high-band are shown in Figures 4.2-9, 4.2-10, and 4.2-11, respectively.

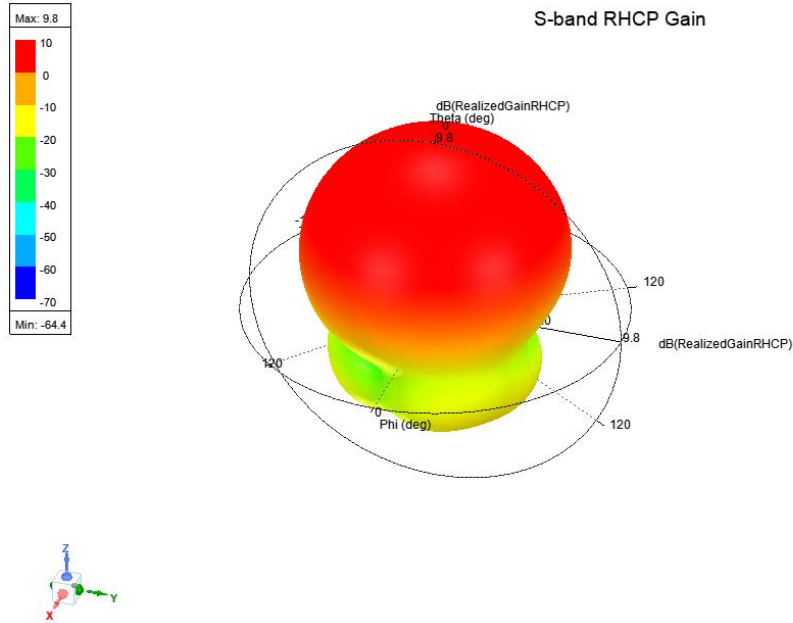


Figure 4.2-9 Integrated S-band RHCP 3D polar radiation pattern (2200 MHz)

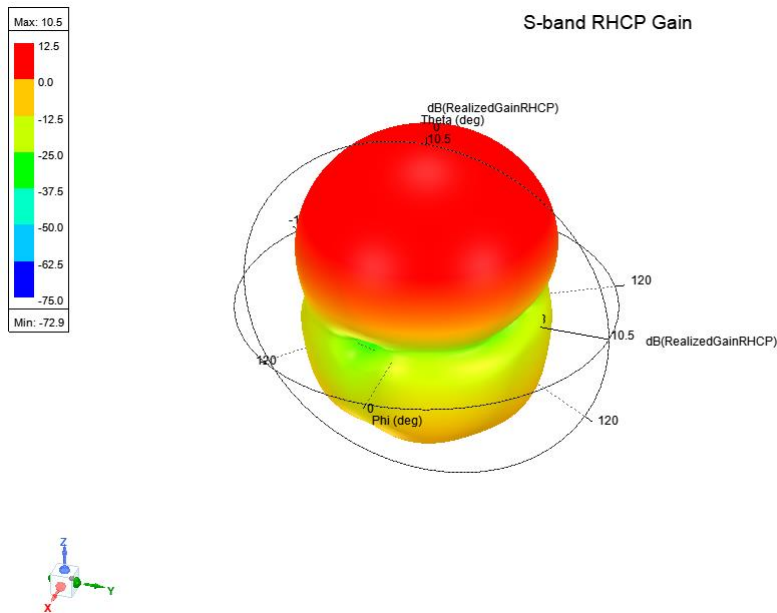


Figure 4.2-10 Integrated S-band RHCP 3D polar radiation pattern (2350 MHz)

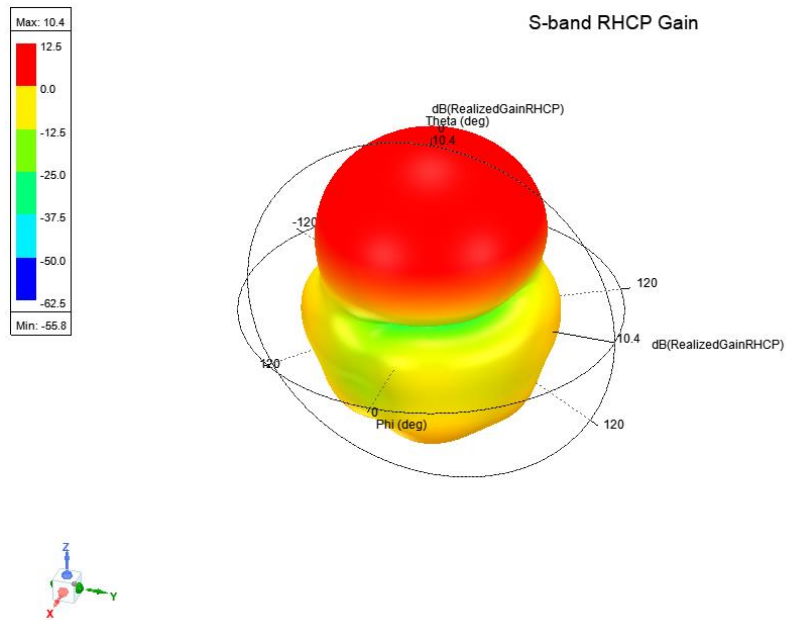


Figure 4.2-11 Integrated S-band RHCP 3D polar radiation pattern (2500 MHz)

The integrated S-band LHCP 3D polar radiation pattern for low-, mid-, and high-band are shown in Figures 4.2-12, 4.2-13, and 4.2-14, respectively.

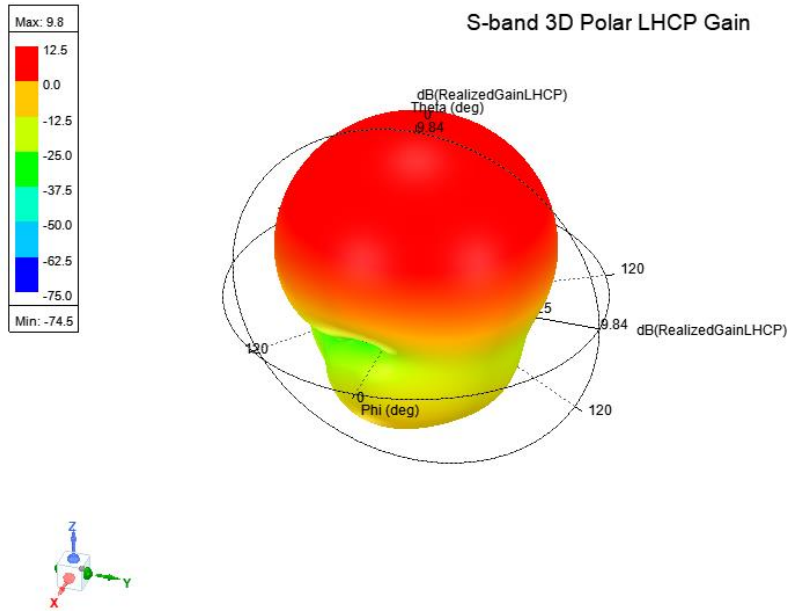


Figure 4.2-12 Integrated S-band LHCP 3D polar radiation pattern (2200 MHz)

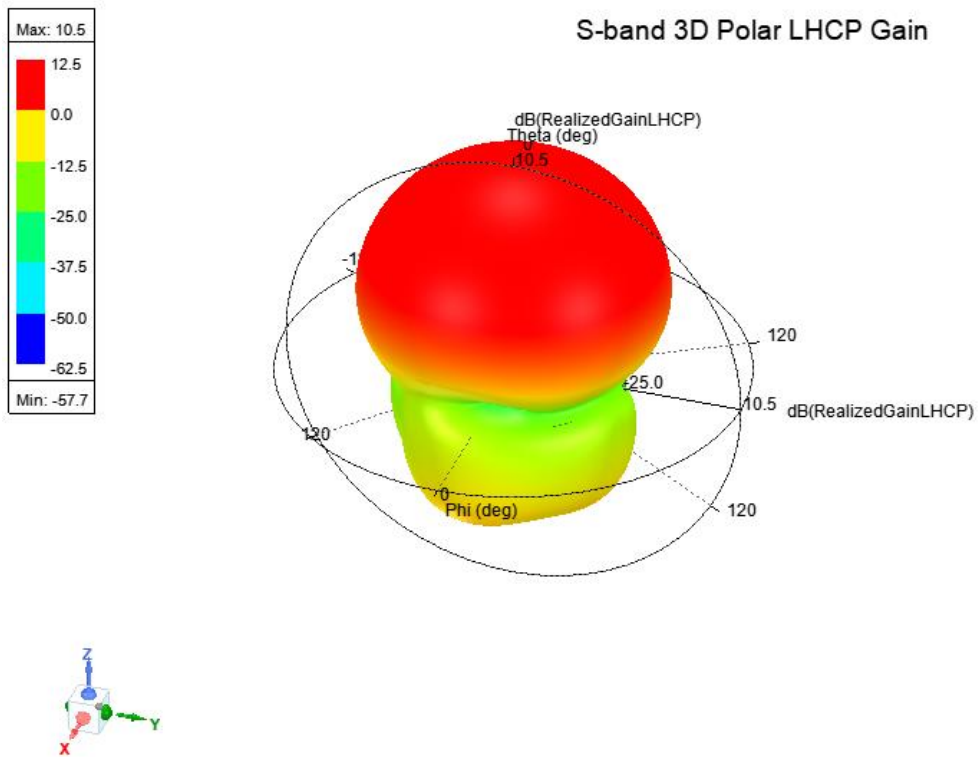


Figure 4.2-13 Integrated S-band LHCP 3D polar radiation pattern (2350 MHz)



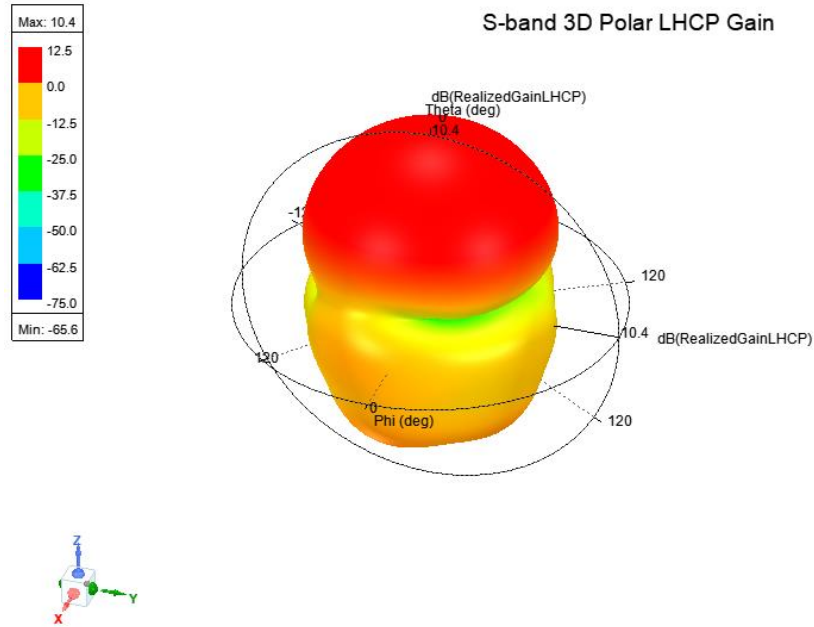


Figure 4.2-14 Integrated S-band LHCP 3D polar radiation pattern (2500 MHz)

The integrated S-band RHCP 2D pattern ( $\phi = 0^\circ, 90^\circ$ ) is plotted for low-, mid-, and high-band in Figures 4.2-15, 4.2-16, and 4.2-17, respectively, with the corresponding 3 dB (half-power) beamwidths.

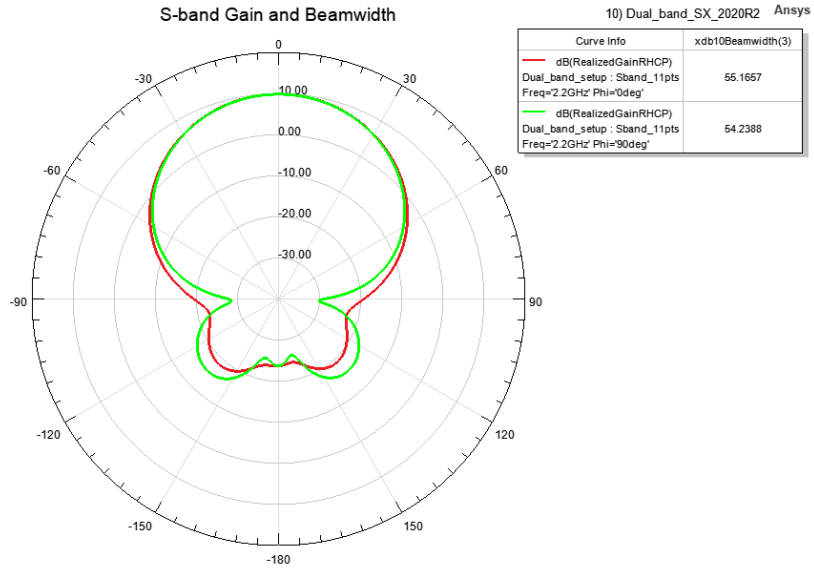


Figure 4.2-15 Integrated S-band RHCP 2D pattern ( $\phi = 0^\circ, 90^\circ$ ) at 2200 MHz with table giving the corresponding 3dB beamwidths.

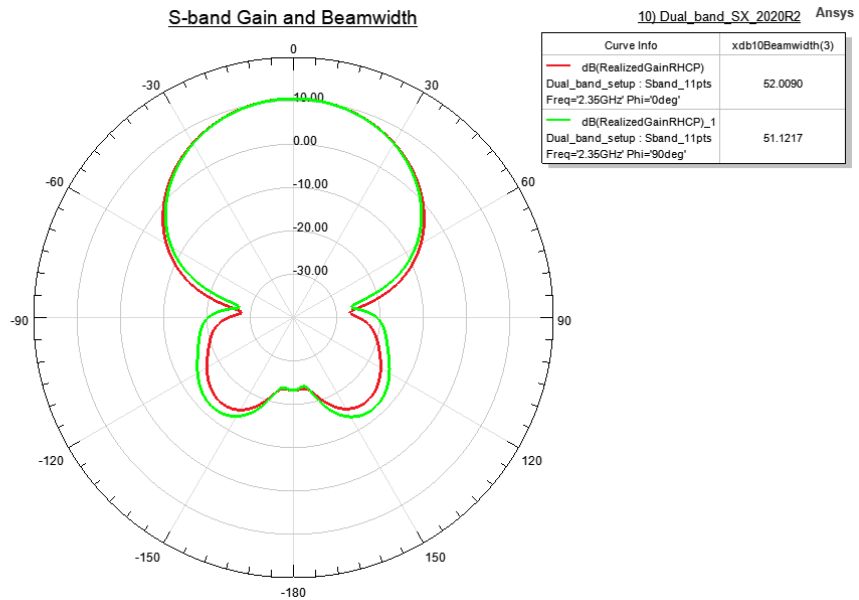


Figure 4.2-16 Integrated S-band RHCP 2D pattern ( $\phi = 0^\circ, 90^\circ$ ) at 2350 MHz with table giving the corresponding 3dB beamwidths.

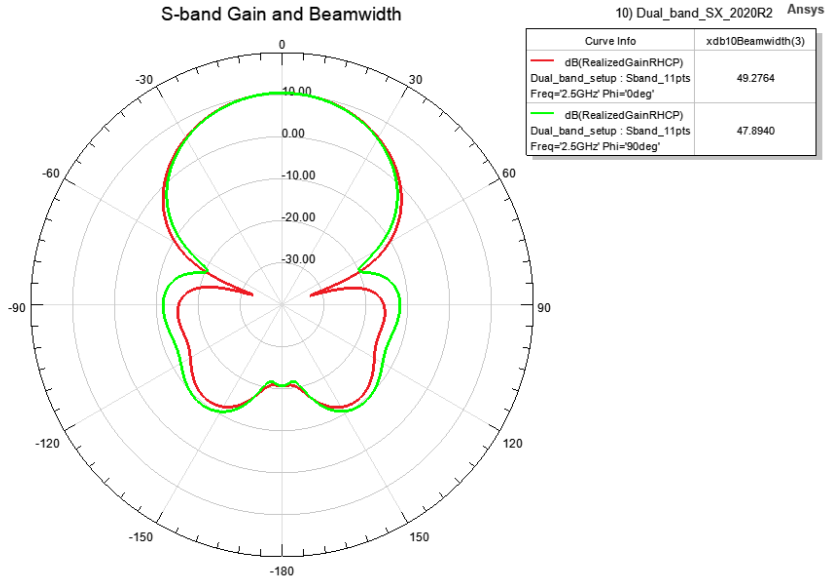


Figure 4.2-17 Integrated S-band RHCP 2D pattern ( $\phi = 0^\circ, 90^\circ$ ) at 2500 MHz with table giving the corresponding 3dB beamwidths.

The integrated S-band LHCP 2D patterns ( $\phi = 0^\circ, 90^\circ$ ) are plotted in Figure 4.2-18, -19, and -20, respectively, with the corresponding 3 dB (half-power) beamwidths.

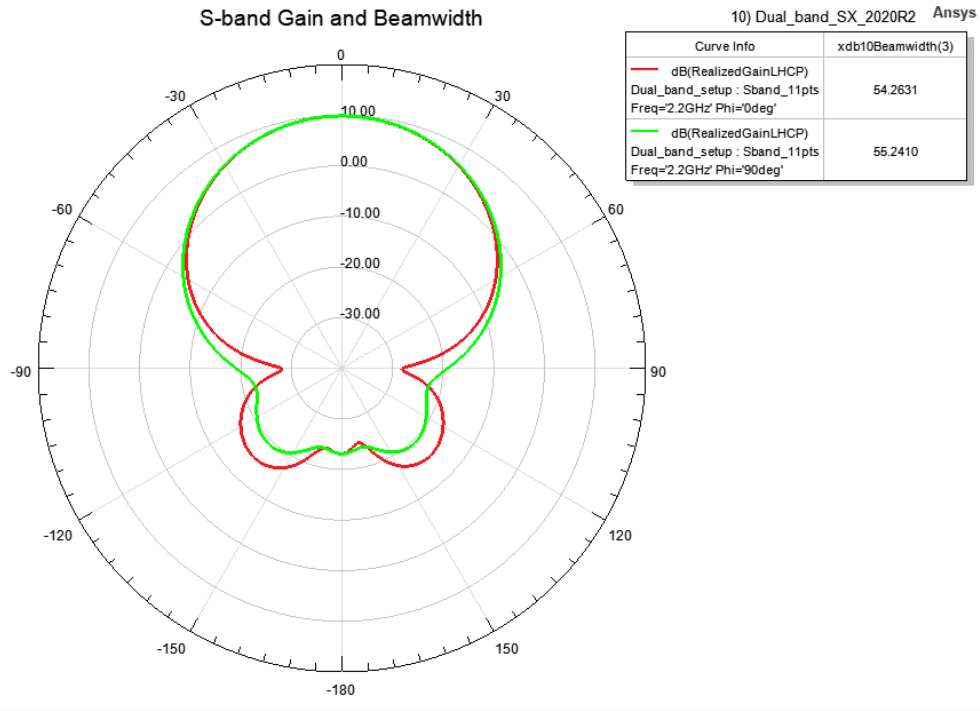


Figure 4.2-18 Integrated S-band LHCP 2D pattern ( $\phi = 0^\circ, 90^\circ$ ) at 2200 MHz with table giving the corresponding 3dB beamwidths.

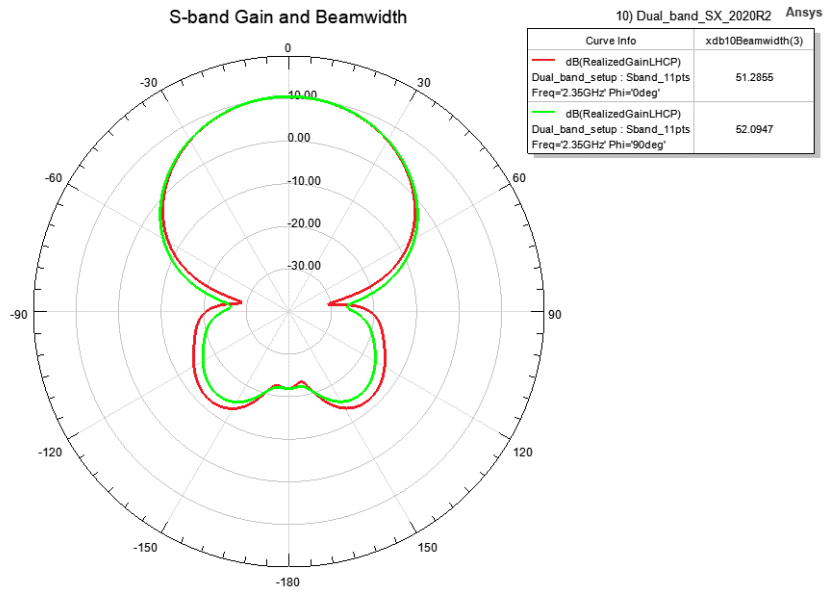


Figure 4.2-19 Integrated S-band LHCP 2D pattern ( $\phi = 0^\circ, 90^\circ$ ) at 2350 MHz with table giving the corresponding 3dB beamwidths.

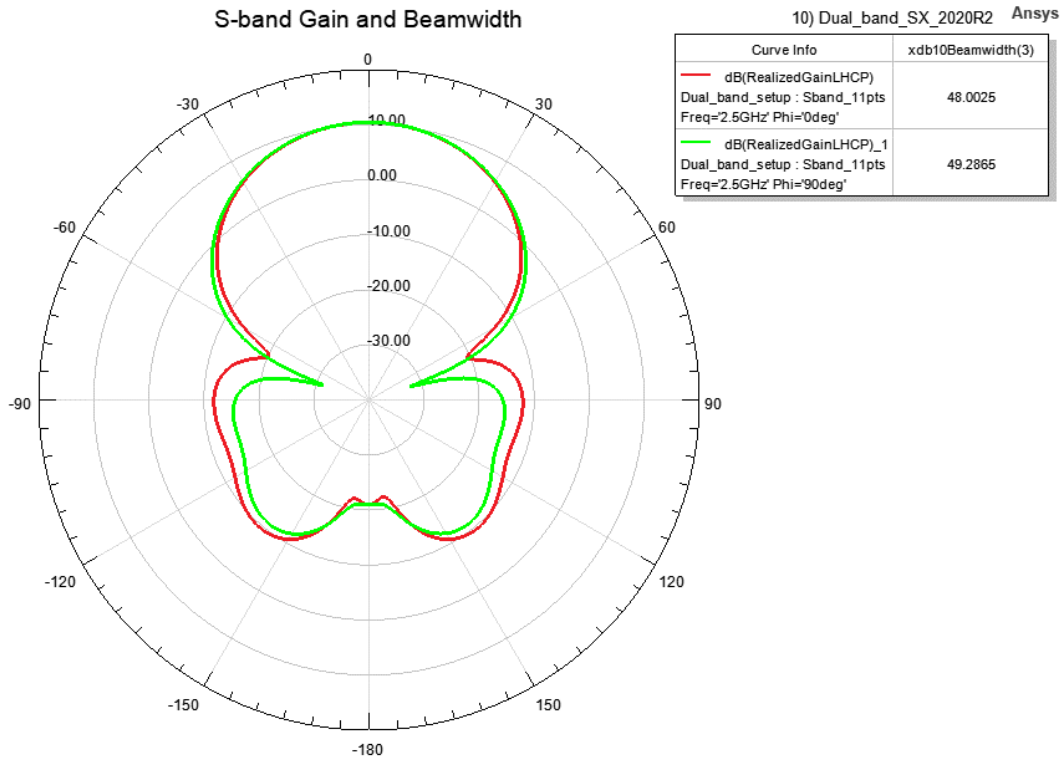


Figure 4.2-20 Integrated S-band LHCP 2D pattern ( $\phi = 0^\circ, 90^\circ$ ) at 2500 MHz with table giving the corresponding 3dB beamwidths.

### 4.3 Aligning Phase Centers for Integrated Dual S/X Band Horns

For proper dual-band operation it is necessary to align the phase centers for the S-band and X-band horns. The phase center is defined as the point from which the electromagnetic radiation spreads spherically outward, with the phase of the signal being equal at any point on the sphere.

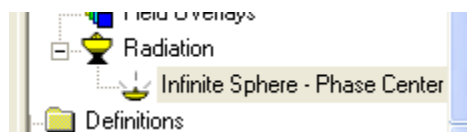
It is possible to determine phase center in HFSS using Optimetrics. The technique involves the following tasks [7]:

1. Define a relative coordinate system that uses a post processing variable.

This allows the variable value to change the definition of the coordinate system and thereby change a solved solution without invalidating it.

2. Use a relative coordinate system in a Far field setup calculation.

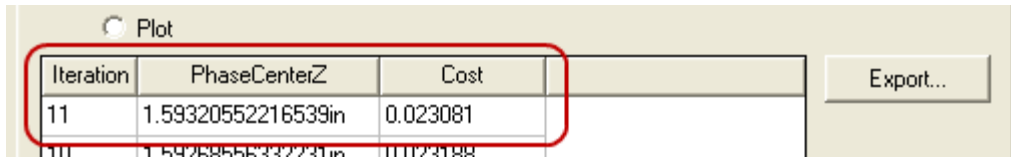
This allows far field quantities to be re-calculated when the relative coordinate system is repositioned (demonstrated in the example by changing the value of the PhaseCenterZ variable), without re-simulation.



The far field setup will also limit the angular range of the sweeping intrinsic ( $\phi$  or  $\theta$ ).

3. Create an optimization setup to search for the phase center. The search will be efficient if you have a rough idea on the location of the phase center. The expression to be optimized is the peak to peak continuous angle of the quantity rEPhi. (The electric field of this antenna is Phi polarized.)
4. Analyze the Optimization setup and view results via the View Analysis Result dialog.

The Z coordinate of the phase center will be the value of the post processing variable when Cost is at minimum.



The phase center of each of the horns was computed using the methodology described above. The results are indicated in Figure 4.3-1 and Table 4.3-1.

Frequency band	PhaseCenterZ	Coordinate system
S-band phase center	8.25638 inches	RelativePhaseCenterZ
X-band phase center	8.25638 inches	RelativePhaseCenterZ

Table 4.3-1 Phase Center Alignment

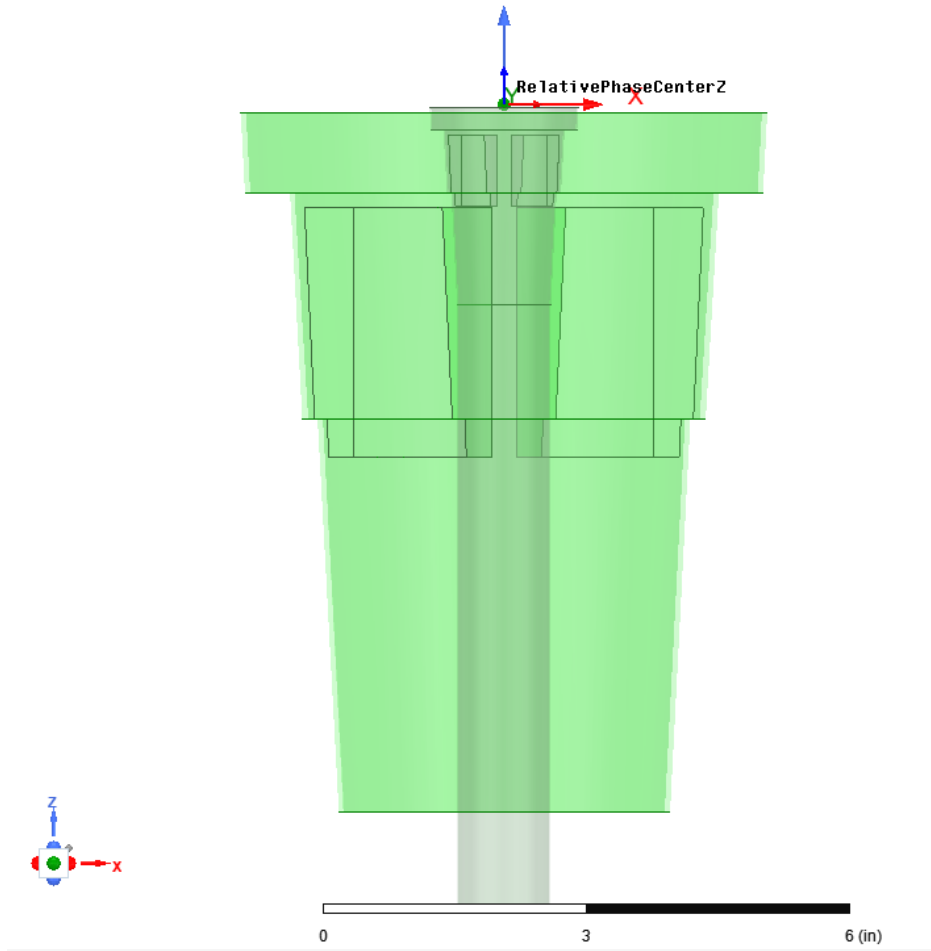


Figure 4.3-1 Phase center alignment



#### 4.4 Aperture Efficiency

A Matlab script [8] was used to calculate the aperture efficiency of the integrated dual S/X band feed illuminating a parabolic reflector antenna having a focal length to diameter (F/D) ratio of 0.35 (the F/D for the reflector located at Arizona State University). Aperture efficiency is generally the product of the [9]:

1. fraction of the total power that is radiated by the feed, intercepted, and collimated by the reflecting surface (generally known as *spillover efficiency*)
2. uniformity of the amplitude distribution of the feed pattern over the surface of the reflector (generally known as *taper efficiency*).
3. phase uniformity of the field over the aperture plan (generally known as *phase efficiency*)
4. polarization uniformity of the field over the aperture plane (generally known as *polarization efficiency*)
5. *blockage efficiency*
6. *random error efficiency* over the reflector surface

The Matlab script (see Appendix A) calculates and plots for comparison an ideal feed pattern based on Eqs. (15-56), (15-57), and (15-58) found on page 902 of Balanis [9] with  $n = 2$ . The ideal feed is based on a class of feeds considered by Silver [10] on the basis that (1) closed form solutions can be obtained, and (2) they often are used to

represent a major part of the main lobe of any many practical antennas. The closed form expression for  $n = 2$  is found in Eq. (15-59a) in Balanis. Figure 15.20a on page 903 of Balanis (reproduced in Figure 4.4-1) plots the Aperture Efficiency for  $n = 2, 4, 6, 8$  vs. Reflector half-angle and F/D.

It is seen in Figure 4.4-1 that for F/D of 0.35, the  $n = 2$  ideal pattern is the closest to achieving the maximum aperture efficiency (close to 80%). It is also observed that as the F/D gets smaller, the reflector half-angle becomes greater. Thus, to achieve maximum aperture efficiency for F/D = 0.35 requires a reflector half-angle of greater than  $70^\circ$ .

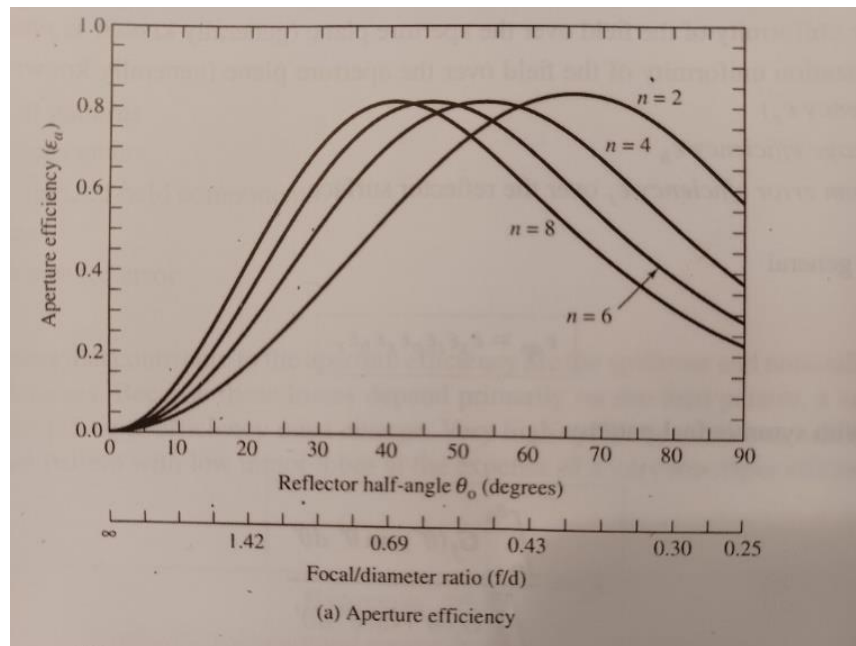


Figure 4-4-1 Aperture Efficiency vs. Reflector half-angle and focal/diameter ratio

The Matlab script plots (see Figure 4.4-2 for illustration) the ideal pattern for  $n = 2$  and the calculated pattern and outputs the calculated aperture efficiency for each.

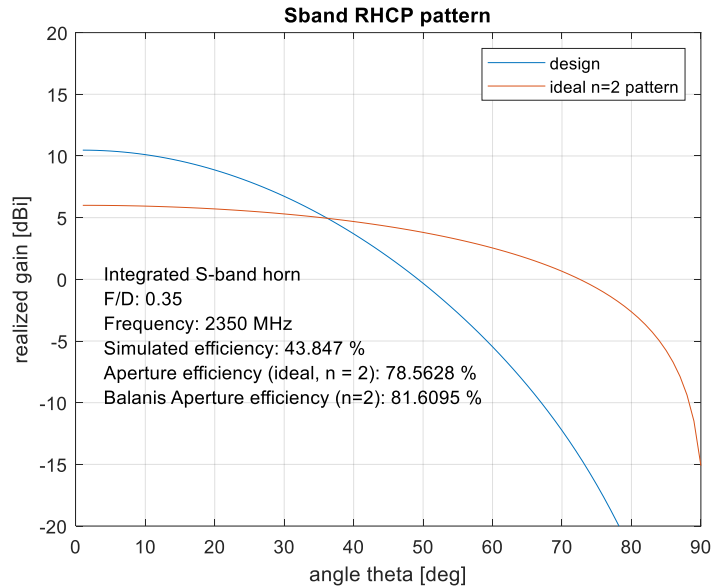


Figure 4.4-2 S-band horn and ideal n=2 Feed patterns and aperture efficiency

The inputs to the Matlab script are the calculated 2D far-field E- and H- plane radiation patterns as a function of angle Theta at the frequency of interest. The calculation focuses on the pattern from  $\theta = 0^\circ$  to  $\theta = 90^\circ$  offset from boresight. For  $F/D = 0.35$ , the aperture efficiency for the ideal  $n = 2$  pattern obtained using the script is 78.6%. The closed-form solution (Balanis equation (15-59a)) predicts an efficiency of 81.6%.

It is seen in Figure 4.4-2 that the S-band horn does not achieve the ideal aperture efficiency for  $F/D = 0.35$ . The aperture efficiency depends on the horn pattern. To change the horn pattern would require adjusting the opening of the horn (wider opening, narrower pattern, and vice versa). The aperture efficiency for the S-band horn and X-band horn is plotted vs.  $F/D$  in Figure 4.4-3. It is seen that the S-band horn is best matched to a reflector with  $F/D = 0.5$ , whereas the X-band horn is best matched to a

reflector with  $F/D = 0.4$ . It is left as a future exercise to optimize the two horns to achieve the ideal aperture efficiency for the same  $F/D$ .

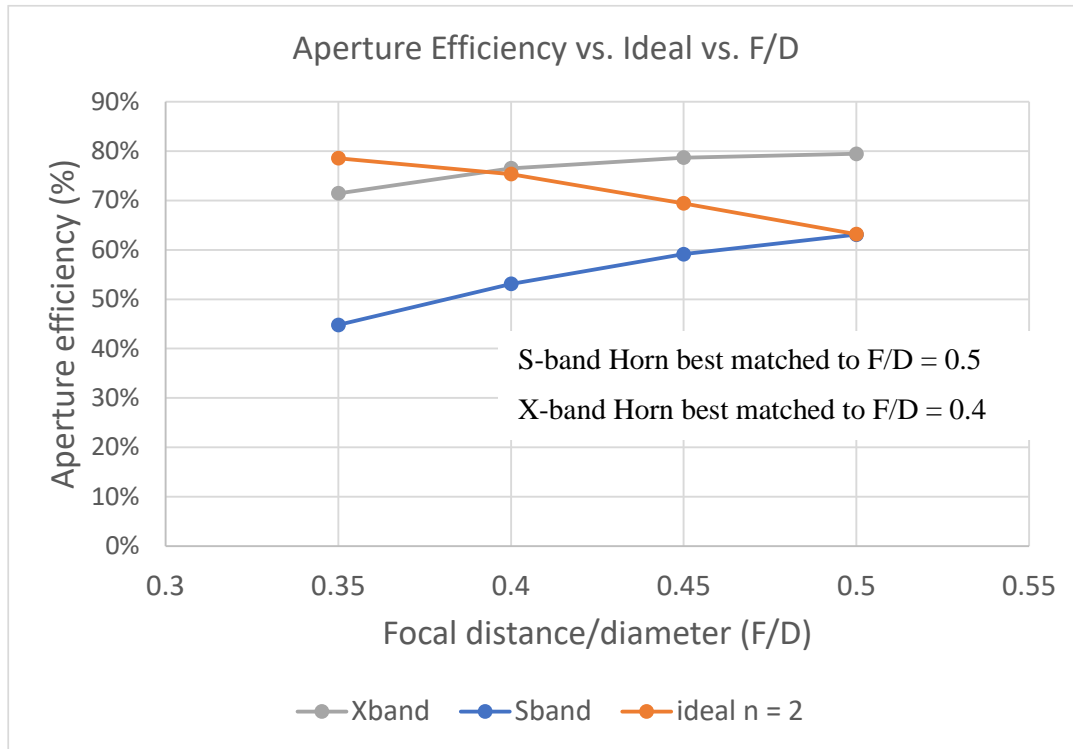


Figure 4.4-3 S-Band and X-band Aperture Efficiency (mid-band) vs.  $F/D$

The 2D pattern cuts ( $\theta = 0^\circ$  to  $90^\circ$ ) and calculated aperture efficiency are plotted for X-band low-, mid-, and high-band in Figures 4.4-4 through 4.4-9, respectively, for  $F/D = 0.35$ . The calculated efficiency for the present design is compared to that of the ideal feed pattern, with  $n = 2$ , using both integration and closed-form approximate solution (Balanis [9]).

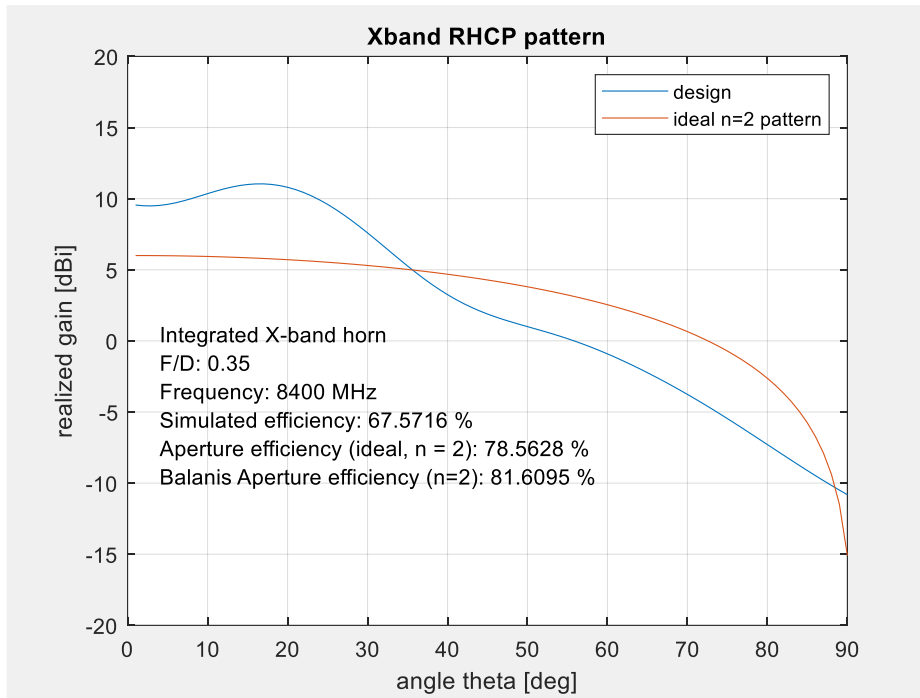


Figure 4.4-4 Aperture efficiency and 2D pattern, X-band, RHCP, 8400 MHz

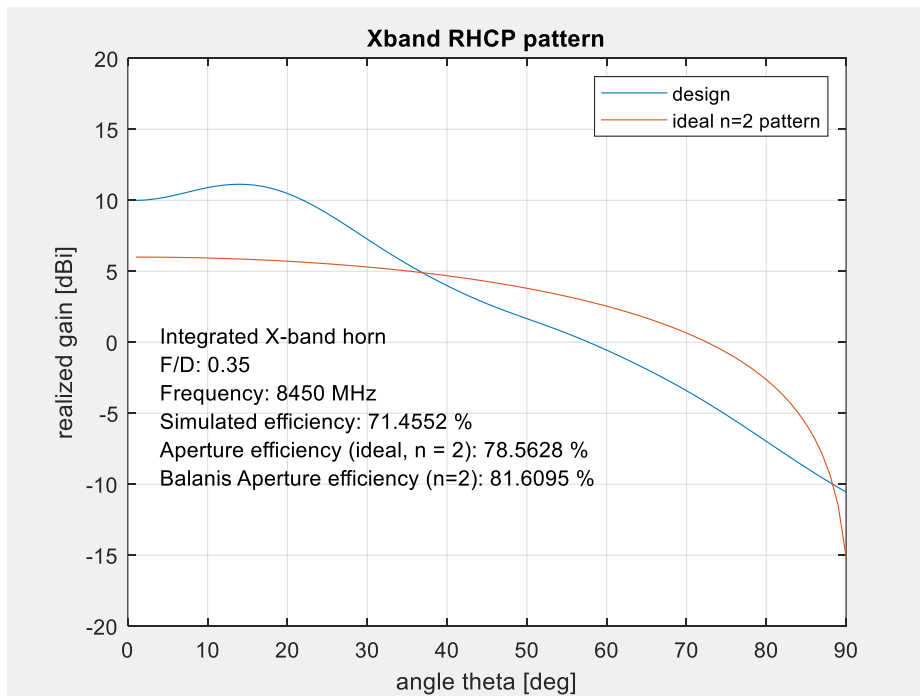


Figure 4.4-5 Aperture efficiency and 2D pattern, X-band, RHCP, 8450 MHz

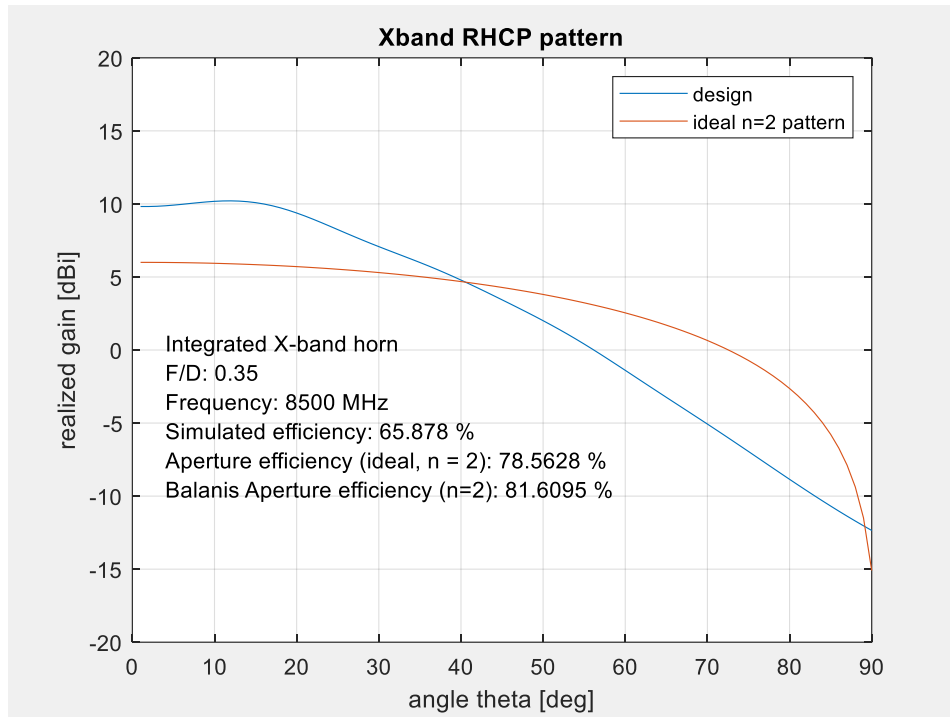


Figure 4.4-6 Aperture efficiency and 2D pattern, X-band, RHCP, 8500 MHz

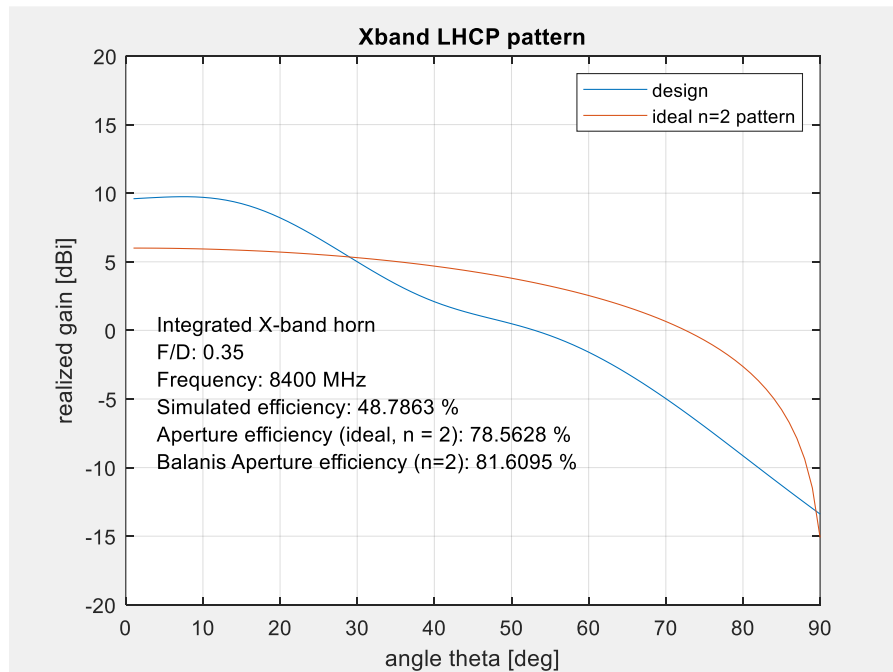


Figure 4.4-7 Aperture efficiency and 2D pattern, X-band, LHCP, 8400 MHz

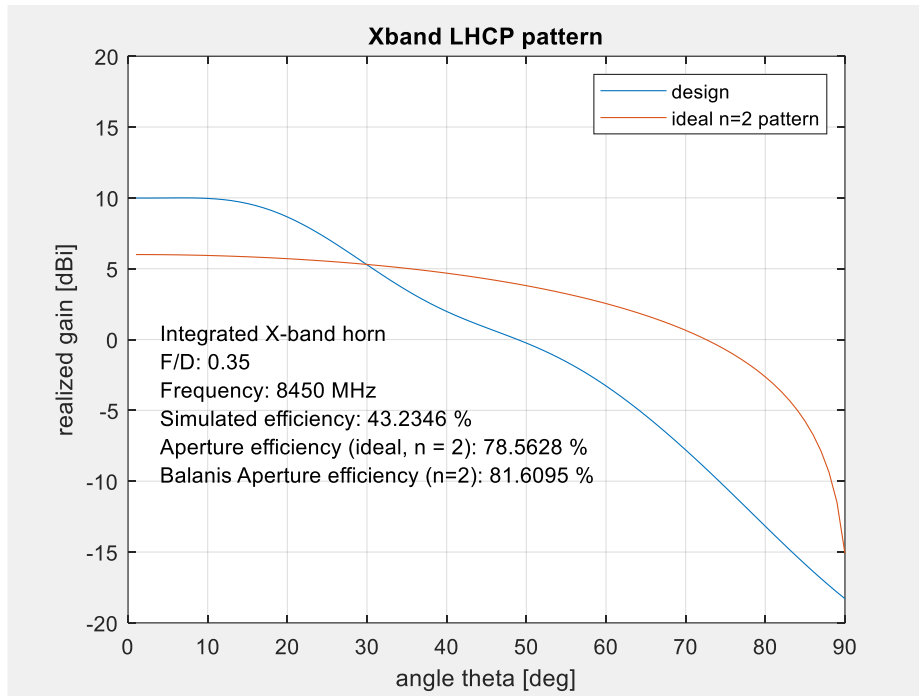


Figure 4.4-8 Aperture efficiency and 2D pattern, X-band, LHCP, 8450 MHz

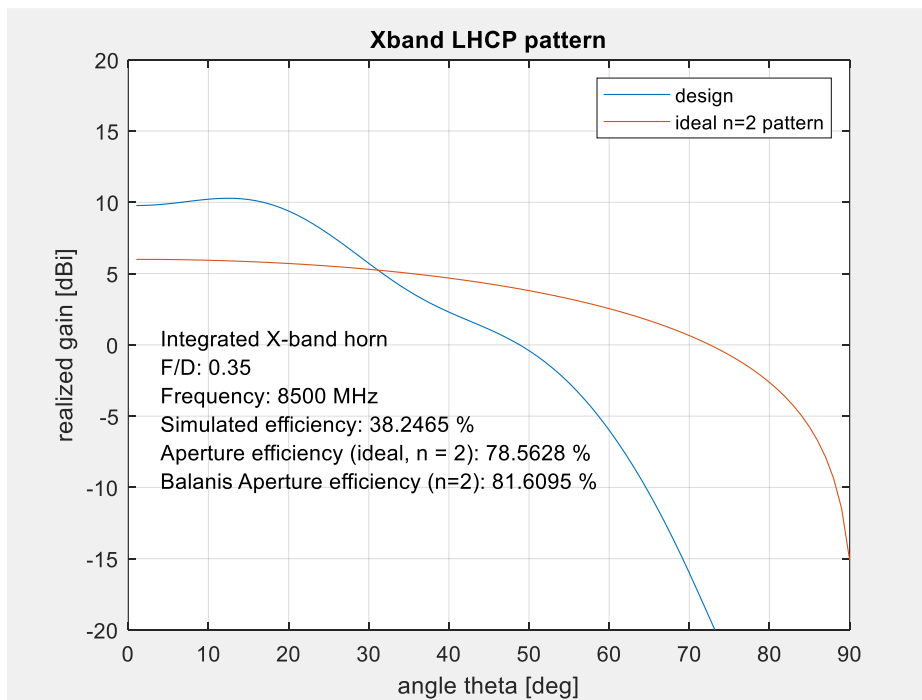


Figure 4.4-9 Aperture efficiency and 2D pattern, X-band, LHCP, 8450 MHz

The 2D pattern cuts and calculated aperture efficiency are plotted for S-band low-, mid-, and high-band in Figures 4.4-10 through 4.4-15, respectively, for  $F/D = 0.35$ . The calculated efficiency for the present design is compared to that of an ideal feed pattern, with  $n = 2$ , using both integration and closed-form approximate solution (Balanis [9]).

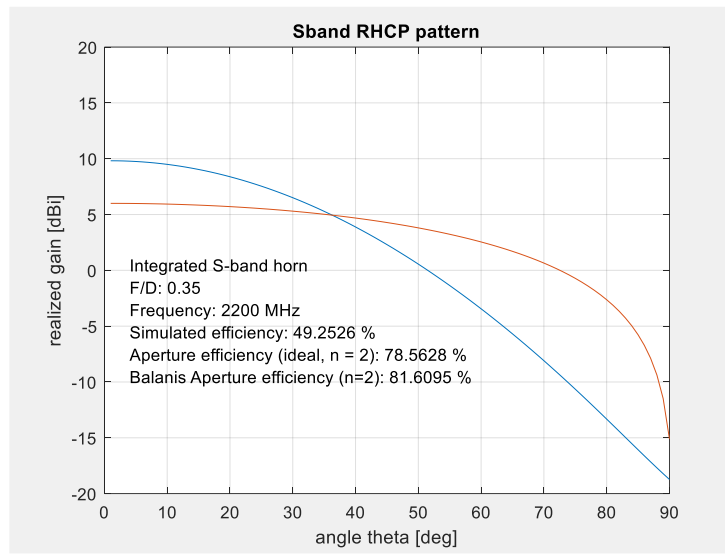


Figure 4.4-10 Aperture efficiency and 2D pattern, S-band, RHCP, 2200 MHz

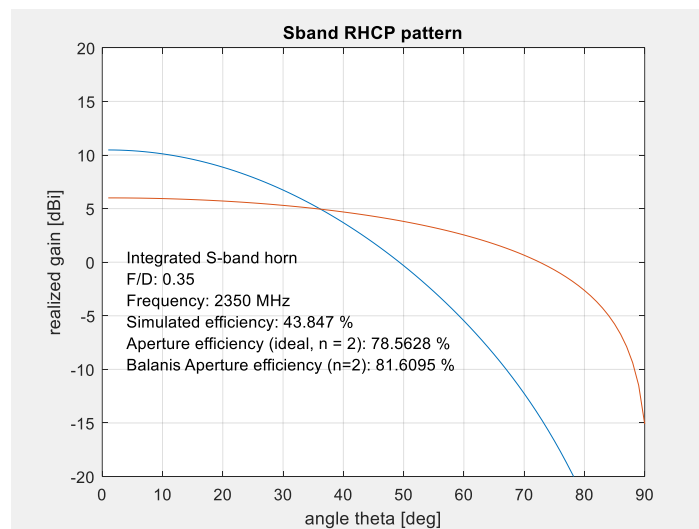


Figure 4.4-11 Aperture efficiency and 2D pattern, S-band, RHCP, 2350 MHz



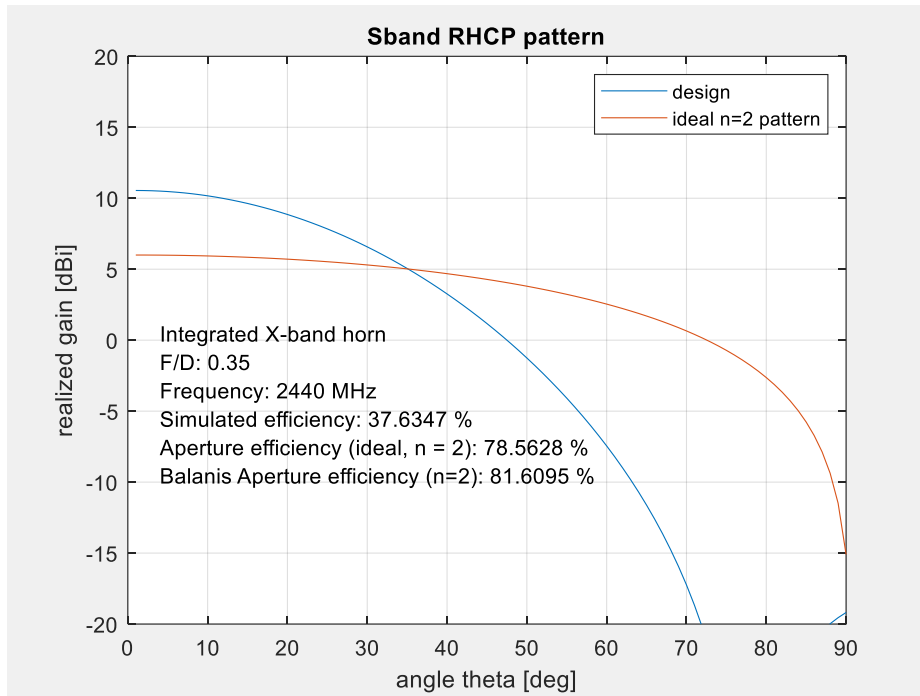


Figure 4.412 Aperture efficiency and 2D pattern, S-band, RHCP, 2440 MHz

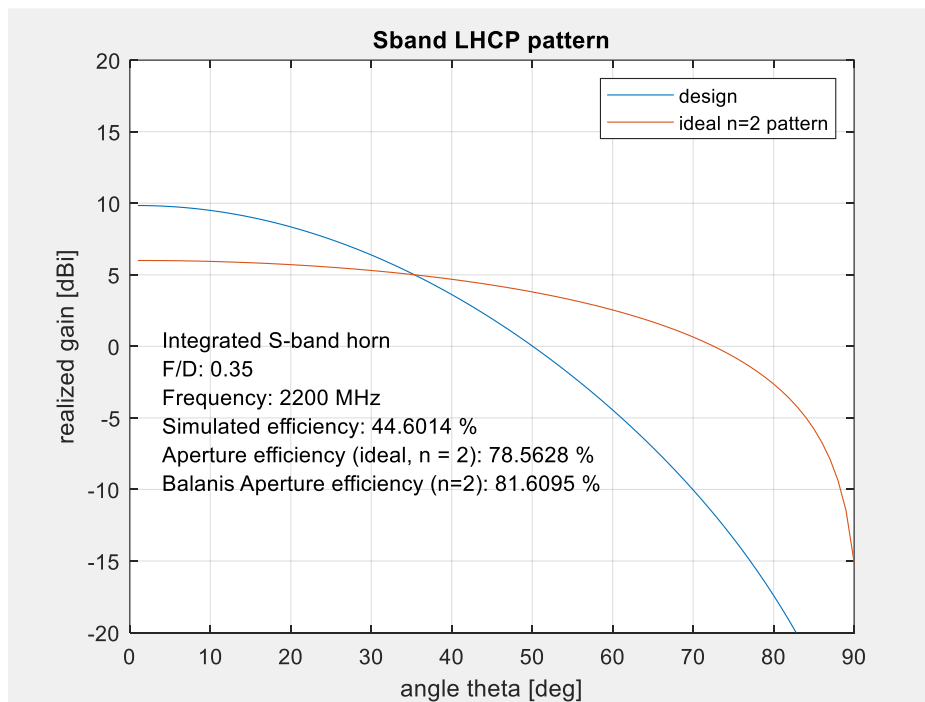


Figure 4.4-13 Aperture efficiency and 2D pattern, S-band, LHCP, 2200 MHz

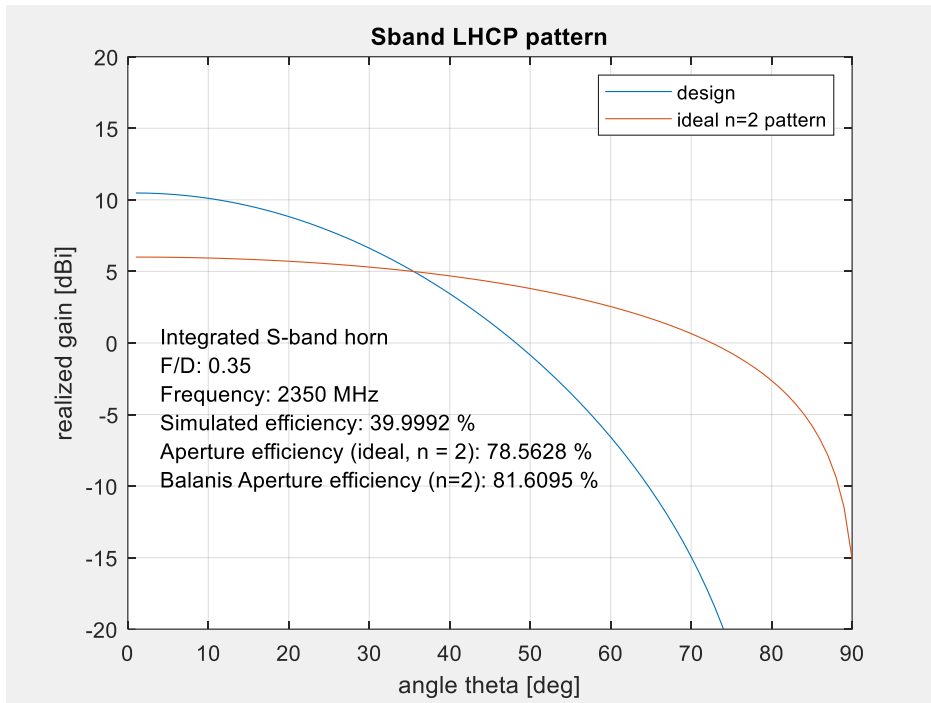


Figure 4.4-14 Aperture efficiency and 2D pattern, S-band, LHCP, 2350 MHz

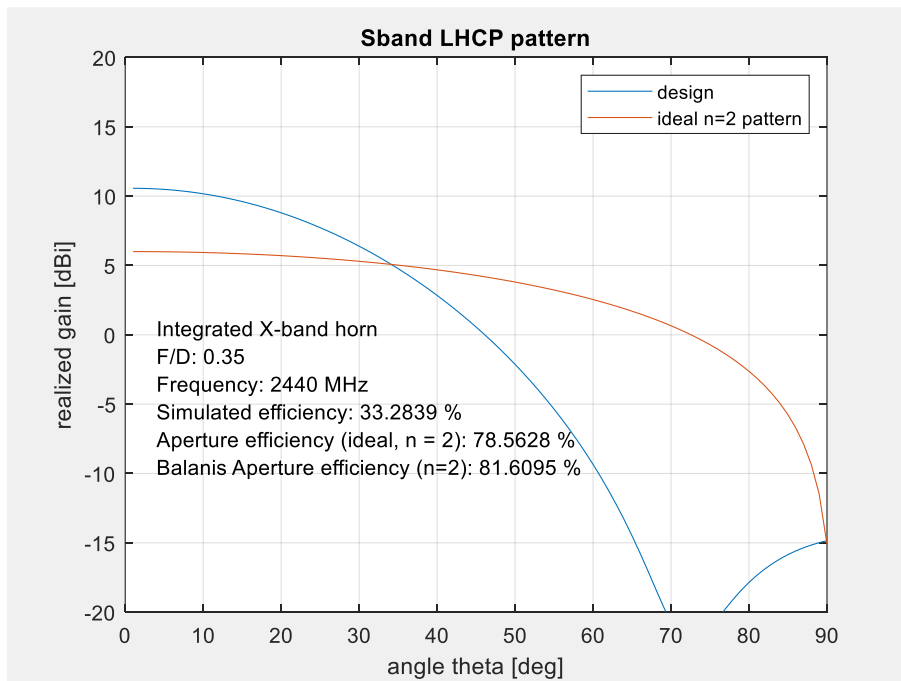


Figure 4.4-15 Aperture efficiency and 2D pattern, S-band, LHCP, 2440 MHz

#### 4.5 Dual Coax to Circular Waveguide Transition

To excite the two circular waveguides, a dual orthogonal coax to circular waveguide transition must be designed for each frequency band and integrated into the dual horn design.

A number of textbook sections and articles (see P. Wade [11], R.E. Collin [12], Ramo, Whinnery, and van Duzer [13], Zhu, Williamson, and Neve [14]) address single coax to circular waveguide transitions. One paper that describes a dual RH/LH circular polarized Orthomode Transducer (OMT) feed is Hassan, Mohamed, et al [15], as shown in Figure 4.5-1.

The dual S/X band nature of the present design imposes significant constraints on the kinds of approaches that can be considered. In particular, one must take into consideration the presence of the X-band waveguide that acts as a center conductor at S-band. The design of this feed is beyond the scope of this thesis, but would be very appropriate for future work.

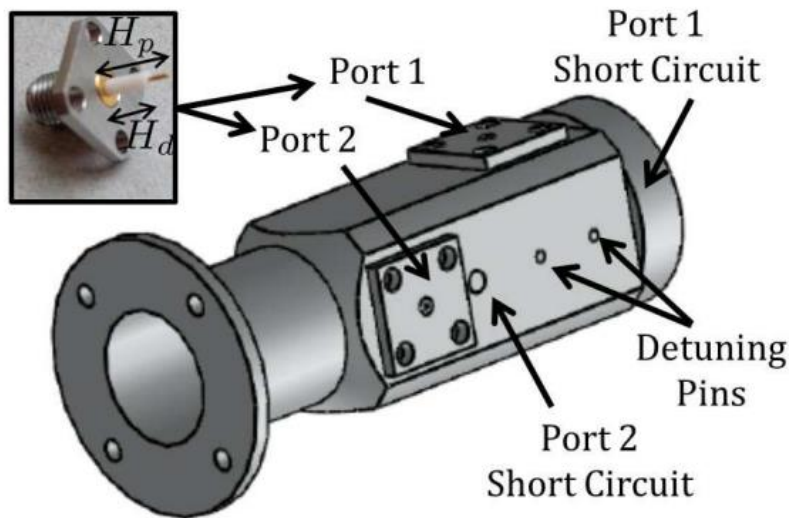


Figure 4.5-1 Conceptual dual polarized OMT feed proposed by Hassan, et al [15]

## CHAPTER 5

### CONCLUSION AND FUTURE WORK

In this thesis, a Dual S/X Band Circular Polarized (CP) feed and polarizer has been designed and simulated using Ansys HFSS. The design features what is known as the “Spread-Squeeze” polarizer, a technique in which “bumps” placed at a  $45^\circ$  angle to the incident wave convert the polarization from linear to circular, and vice versa. This technique offers a number of advantages, including compact size, ease of manufacturing, and lower loss (lower noise figure for receive-only applications).

The S-band horn design is such that it achieves the ideal ( $n = 2$ ) aperture efficiency for a parabolic reflector  $F/D$  of 0.5, whereas the X-band horn achieves the ideal ( $n = 2$ ) aperture efficiency for  $F/D$  of 0.4. Achieving the ideal efficiency for  $F/D = 0.5$  for both horns should be achievable and applicable to many reflectors available on the market today. This is left as future work.

Future work would also entail designing dual orthogonal coaxial to circular waveguide transitions for each frequency band and integrating the resulting feed with the dual horn design. The design of the S-band waveguide probes needs to take into account potential interaction and mechanical interference with the X-band waveguide (S-band center conductor) while simultaneously achieving good reflection, isolation, and transmission performance in a compact fit-form. Ultimately, prototyping this design, optimizing the performance of the manufactured unit, and testing with parabolic dishes having  $F/D$  ranging from 0.35 to 0.50, will be needed.

## REFERENCES

- [1] "Circular Polarization vs. Linear Polarization," Intelsat, [Online]. Available: <https://pdf4pro.com/view/circular-polarization-vs-linear-polarization-intelsat-24708.html>. [Accessed 15 August 2020].
- [2] B. Subbarao and V. Fusco, "Compact Coaxial-Fed Polarizer," *IEEE Antennas and Wireless Propagation Letters*, Vol. 3, pp. 145-147, 2004.
- [3] H. Schrank, "The "Spread-Squeeze" Waveguide Polarizer," *IEEE Antennas and Propagation Society Newsletter*, p. 12, October 1984.
- [4] R. Galuscak, "A Simple S/X Dual-Band Coaxial Feed for Satellite Communication," [Online]. Available: [http://www.om6aa.eu/A\\_Simple\\_S\\_X\\_Dual\\_Band\\_Coaxial\\_Feed\\_for\\_Satellite\\_Communication\\_FV.pdf](http://www.om6aa.eu/A_Simple_S_X_Dual_Band_Coaxial_Feed_for_Satellite_Communication_FV.pdf). [Accessed 25 September 2021].
- [5] A. Oliver, P. Clarricoats, A. A. Kishk and L. Shafai, *Microwave Horns and Feeds*, New York: IEEE, 1994.
- [6] N. Marcuvitz, *Waveguide Handbook*, McGraw-Hill , 2009.
- [7] Ansys Incorporated, "Determining Phase Center Using Optimetrics (Ansys Electronics 2021 R2)," Ansys, 2021. [Online]. Available: <https://sudonull.com/post/7587-Antenna-Phase-Center-Antenna-and-its-search-in-Ansys-HFSS>.
- [8] J. T. Aberle, *Aperture Efficiency Matlab function*, 2004.
- [9] C. A. Balanis, "Front-Fed Parabolic Reflector," in *Antenna Theory, Analysis and Design, 4th ed.*, Hoboken, New Jersey, John Wiley & Sons, 2016, pp. 887-915.
- [10] S. Silver, *Microwave Antenna Theory and Design (MIT Radiation Lab Series, Vol. 12)*, New York: McGraw-Hill, 1949.
- [11] P. Wade, "Understanding Circular Waveguide--Experimentally," *QEX*, pp. 37-48, Jan/Feb 2001.
- [12] R. E. Collin, "Section 7.1, Excitation of Waveguides and Cavities," in *Field Theory of Guided Waves -- 2ed*, Piscataway, NJ, IEEE Press, 1990, pp. 471-483.
- [13] S. Ramo, J. Whinnery and T. van Duzer, "Section 8.11, Waveguides with Cylindrical Conducting Boundaries," in *Fields and Waves in Communication Electronics - 3ed*, New York, John Wiley & Sons, Inc., 1994, pp. 434-438.

- [14] Q. C. Zhu, A. G. Williamson and M. J. Neve, "Design of Coaxial Line-to-Circular Waveguide Transitions," in *International Microwave Symposium*, Boston, 2009.
- [15] M. A. Moharram, A. Mahmoud and A. A. Kishk, "A Simple Coaxial to Circular Waveguide OMT for Low Power Dual Polarized Antenna Applications," *IEEE Transactions On Microwave Theory And Techniques*, no. 10.1109/TMTT.2017.2734089, pp. 1-8, 2017.

## APPENDIX A

### MATLAB SCRIPT - APERTURE EFFICIENCY

## Matlab script for computing aperture efficiency and comparing to aperture

efficiency for ideal feed pattern for  $n = 2$ .

```
% test_apert_eff.m
% Test function for computing aperture efficiency using an
idealized feed
% pattern that is a good approximation to expected horn
patterns
clear all
close all
clc
%% Given
FD = 0.35
freq = 2340;

% fn1 = 'Sband_iso_RHCP_2350_MHz_fd9.csv';
% fn1 = 'Xband_LHCP_8500.csv';
fn1 = 'Sband_Gain_Beamwidth_2340.csv';
sheet = 1;
% xlRange = 'B2:B362';
xlRange = 'B182:B272';

theta = linspace(0,180,181);
gain_ec = -160*ones(size(theta)); % initialize values to
very small in dB
k = find(theta <= 90);
gain_ec(k) = xlsread(fn1,sheet,xlRange)';
gain_hc = gain_ec;
gain_ec_sim = gain_ec(k);
%% Call function for computing aperture efficiency
eta_ap_sim = apert_eff(FD,theta,freq,gain_ec,gain_hc)

%% Preliminary calculations
theta_0 = 2*acotd(4*FD);

%% Idealized feed pattern
% theta = linspace(0,180,181);
% gain_ec = -160*ones(size(theta)); % initialize values to
very small in dB
% k = find(theta <= 90);
% gain_ec(k) = 10*log10(10*cosd(theta(k)).^4); % Balanis
(15-56, n=4)
```



```

gain_ec(k) = 6*log10(10*cosd(theta(k)).^2); % Balanis (15-
56, n=2) % ideal gain pattern
gain_hc = gain_ec; % ideal gain pattern
gain_ec_ideal_n2 = gain_ec;

%% Call function for computing aperture efficiency
eta_ap_ideal_n2 = apert_eff(FD,theta,freq,gain_ec,gain_hc)

%% Calculate aperture efficiency using Balanis (15-59b,
n=4)
% eta_ap_Bal_n4 = 40*(sind(theta_0/2).^4 +
log(cosd(theta_0/2))).^2 .* cotd(theta_0/2).^2

%% Calculate aperture efficiency using Balanis (15-59a,
n=2)
eta_ap_Bal_n2 = 24*(sind(theta_0/2).^2 +
log(cosd(theta_0/2))).^2 .* cotd(theta_0/2).^2

%% generate plot
plot(gain_ec_sim) % plot simulated gain
hold
plot(gain_ec_ideal_n2) % plot ideal gain, n=2
xlim([0 90])
ylim([-20 20])
grid
title('Sband RHCP pattern')
xlabel('angle theta [deg]')
ylabel('realized gain [dBi]')
txt1 = ['Isolated S-band horn'];
txt2 = ['F/D: ',num2str(FD)];
txt3 = ['Frequency: ',num2str(freq),' MHz'];
txt4 = ['Simulated efficiency: ',num2str(eta_ap_sim*100),'
%'];
txt5 = ['Aperture efficiency (ideal, n = 2):
',num2str(eta_ap_ideal_n2*100),' %'];
txt6 = ['Balanis Aperture efficiency (n=2):
',num2str(eta_ap_Bal_n2*100),' %'];
text(4,0.5,txt1)
text(4,-1.5,txt2)
text(4,-3.5,txt3)

```

```
text(4,-5.5,txt4)
text(4,-7.5,txt5)
text(4,-9.5,txt6)
```

```
function eta_ap = apert_eff(FD,theta,freq,gain_ec,gain_hc)
% function to determine the aperture efficiency of
% reflector antenna
% given F/D ratio and feed pattern
%
% function eta_ap =
% apert_eff(FD,theta,freq,gain_ec,gain_hc)
%
% input variables:
% FD = F/D ratio
% theta = theta points (deg)
% freq = frequency points (MHz)
% gain_ec = co-pol gain in E-plane
% gain_hc = co-pol gain in H-plane
% output variables:
% eta_ap = aperture efficiency as a dimensionless quantity
%
% written by James T. Aberle
% Latest version: 06/30/04

% initialize variables
Nfreqs = length(freq);
Ntheta = length(theta);
dtheta = theta(2) - theta(1);

% convert gain values from dB to dimensionless
G_ec = 10.^(gain_ec/10);
G_hc = 10.^(gain_hc/10);

% average the gain values to remove phi-variation
G_f = (G_ec + G_hc)/2;

% evaluate the subtended angle
theta_0 = 2*acotd(4*FD);

% find those gain values that contribute to illumination
```

```

% use a slight asymmetry to try to make integration more
accurate!
s = find(theta>=-theta_0 & theta<=theta_0+dtheta);

% evaluate the integrand
z = zeros(size(G_f));
for n=1:Nfreqs,
    z(n,:) = sqrt(G_f(n,:)).*abs(tan(pi/180*theta/2));
end

% integrate over cone
zi = trapz(pi/180*theta(s),z(:,s),2);

% compute aperture efficiency
eta_ap = cot(pi/180*theta_0/2)^2*zi.^2;

```